# Hole quantum spintronics in strained germanium heterostructures

Patrick Torresani

Communauté
UNIVERSITÉ Grenoble Alpes

# THÈSE

Pour obtenir le grade de

## DOCTEUR DE la Communauté UNIVERSITÉ GRENOBLE ALPES

Spécialité : **Nanophysique**

Arrêté ministériel : 7 Août 2006

Présentée par


## TORRESANI Patrick


Thèse dirigée par **DE FRANCESCHI Silvano**

préparée au sein du **LaTEQS, du service PHELIQS, de l'Institut NAnosciences et Cryogénie, du CEA Grenoble**
et de **Ecole doctorale de physique**

# Hole quantum spintronics in strained germanium heterostructures

Thèse soutenue publiquement le **14/06/2017**,
devant le jury composé de :

**Prof. Marco Fanciulli**
Università degli Studi di Milano-Bicocca, Président

**Prof. Wilfred van der Wiel**
University of Twente, Rapporteur

**Prof. Stefano Roddaro**
Scuola Normale Superiore Pisa, Rapporteur

**Dr Hermann Sellier**
Institut Neel, Examinateur

**Dr Silvano De Franceschi**
CEA Grenoble, Directeur de thèse

À mes grand-mères…

# Abstract

This thesis focuses on low temperature experiments in germanium based heterostructure in the scope of quantum spintronic. First, theoretical advantages of Ge for quantum spintronic are detailed, specifically the low hyperfine interaction and strong spin orbit coupling expected in Ge. In a second chapter, the theory behind quantum dots and double dots systems is explained, focusing on the aspects necessary to understand the experiments described thereafter, that is to say charging effects in quantum dots and double dots and Pauli spin blockade. The third chapter focuses on spin orbit interaction. Its origin and its effect on energy band diagrams are detailed. This chapter then focuses on consequences of the spin orbit interaction specific to two dimensional germanium heterostructure, that is to say Rashba spin orbit interaction, D'Yakonov Perel spin relaxation mechanism and weak antilocalization.

In the fourth chapter are depicted experiments in Ge/Si core shell nanowires. In these nanowire, a quantum dot form naturally due to contact Schottky barriers and is studied. By the use of electrostatic gates, a double dot system is formed and Pauli spin blockade is revealed.

The fifth chapter reports magneto-transport measurements of a two-dimensional hole gas in a strained Ge/SiGe heterostructure with the quantum well laying at the surface, revealing weak antilocalization. By fitting quantum correction to magneto-conductivity characteristic transport times and spin splitting energy of 2D holes are extracted. Additionally, suppression of weak antilocalization by a magnetic field parallel to the quantum well is reported and this effect is attributed to surface roughness and virtual occupation of unoccupied subbands.

Finally, chapter number six reports measurements of quantization of conductance in strained Ge/SiGe heterostructure with a buried quantum well. First the heterostructure is characterized by means of magneto-conductance measurements in a Hall bar device. Then another device engineered specifically as a quantum point contact is measured and displays steps of conductance. Magnetic field dependance of these steps is measured and an estimation of the g-factor for heavy holes in germanium is extracted.

# Résumé

Le travail exposé dans cette thèse de doctorat présente des expériences à basse température dans le domaine de la spintronique quantique sur des hétérostructures à base de germanium. Tout d'abord, les avantages attendus du germanium pour la spintronique quantique sont exposés, en particulier la faible interaction hyperfine et le fort couplage spin-orbite théoriquement prédits dans le Ge. Dans un second chapitre, la théorie des boites quantiques et systèmes à double boite sont détaillés, en se focalisant sur les concepts nécessaires à la compréhension des expériences décrites plus tard, c'est-à-dire les effets de charge dans les boites quantiques et double boites, ainsi que le blocage de spin de Pauli. Le troisième chapitre s'intéresse à l'interaction spin-orbite. Son origine ainsi que ses effets sur les diagrammes d'énergie de bande sont discutés. Ce chapitre se concentre ensuite sur les conséquences de l'interaction spin-orbite spécifiques aux gaz bidimensionnels de trous dans des hétérostructures de germanium, c'est-à-dire l'interaction spin-orbite Rashba, le mécanisme de relaxation de spin D'Yakonov-Perel ainsi que l'antilocalisation faible.

Le chapitre quatre présente des mesures effectuées sur des nanofils cœur coquille de Ge/Si. Dans ces nanofils une boite quantique se forme naturellement et celui-ci est étudié. Un système à double boite quantiques est ensuite formé par utilisation de grilles électrostatiques, révélant ainsi du blocage de spin de Pauli.

Dans le cinquième chapitre sont détaillés des mesures de magneto-conductance de gas de trous bidimensionnels dans des hétérostructures de Ge/SiGe contraints dont le puit quantique se situe à la surface. Ces mesures montrent de l'antilocalisation faible. Les temps de transport caractéristiques sont extraits ainsi que l'énergie de séparation des trous

2D par ajustement de courbe de la correction à la conductivité due à l'antilocalisation. De plus, les mesures montrent une suppression de l'antilocalisation par un champ magnétique parallèle au puit quantique. Cet effet est attribué à la rugosité de surface ainsi qu'à l'occupation virtuelle de sous-bandes inoccupées.

Finalement, le chapitre six présente des mesures de quantisation de la conductance dans des hétérostructures de Ge/SiGe contraints dont le puit quantique est enterré. Tout d'abord, l'hétérostructure est caractérisée grâce à des mesures de magneto-conductance dans une barre de Hall. Ensuite, un second échantillon dessiné spécialement pour la réalisation de points de contact quantiques est mesuré. Celui-ci montre des marches de conductance. La dépendance en champ magnétique de ces marches est mesurée, permettant ainsi une extraction du facteur gyromagnétique de trous lourds dans du germanium.

# Table of contents

# List of figures

# List of tables

# Introduction

During the second half of the $20^{th}$ century computers have revolutionized the way scientific research is made. The ever increasing computing power available allowed for the simulation of problems of exceptional complexity. Still, as Richard Feynman explained in his famous talk in 1981 [1], a classical computer, being limited to classical physics, will never be a universal computer, that is to say a computer that can be used to simulate any physics problem. In particular, being based on classical physics, classical computers could not properly simulate the quantum world. This would require a quantum computer.

In classical computing, information is encoded in bits. These bits are two levels systems, usually denoted by 0 and 1. On chips, such as CPUs, they are physically implemented by transistors of which the open or closed status are the two levels of the bit. In a quantum computer, these classical bits would be replaced by quantum bits or qubits. Instead of a classical two level system, that can be 0 or 1, a qubit would rely on a quantum two level system, that can be in any superposition of the two levels.

Qubits can theoretically be realized with any quantum two level system, but a quantum computer should be based on qubits that respects the 5 DiVincenzo's criteria exposed in 2000 [2]. In 1998 Loss and DiVincenzo had already made a proposal for such a system. The idea was to use the spin of an electron in a quantum dot as a two level system [3], thus providing an efficient way to do two qubits gates (one of DiVincenzo's criteria) by the simple use of electrical gating.

This proposal led to an increase in interest in the field of quantum spintronic. Research was performed in order to engineer qubits in different systems, mainly III-V materials such as GaAs two dimensional electron gas [4] or InAs nanowires [5].

But not every qubit are equal. Indeed, in order to create a fault tolerant quantum computing system, one has to use quantum error correction codes [6] that require that the qubit states lifetimes are longer than the operation gate times. As the hyperfine interaction is the main reason for spin decoherence, more and more interest has been seen for group IV materials such as Ge and Si recently for which almost all natural isotopes have no nuclear spins.

The prospect of realizing a quantum computer based on spin qubits then require the use of a material in which spin manipulation is fast and coherence time is long. Systems based on strained germanium is expected to present such characteristics. The aim of this thesis is to present experiments that will tend to bring new information on the validity of these claims.

The outline of this thesis will be as follows. The first chapter will try to highlight the advantages of Germanium in the field of quantum spintronic, focusing around the low hyperfine interaction and strong spin orbit coupling. The second chapter focuses on the theory of quantum dots and double quantum dots systems. This chapter is limited to the concepts required for a correct understanding of the results obtained in the following chapters, that is to say charging effect in quantum dots and double dots systems and Pauli spin blockade. Chapter three describes the theory of spin orbit interaction. Similarly to chapter two, this chapter does not pretend to be a review on spin orbit but only highlights the elements of this theory that permit to describe the systems described in the following chapters. In chapter four, experiments on Ge/Si core/shell nanowires are described. In these nanowire, a quantum dot form naturally due to contact Schottky barriers and is studied. By the use of electrostatic gates, a double dot system is formed and Pauli spin blockade is revealed. The fifth chapter reports magneto-transport measurements of a two-dimensional hole gas in a strained Ge/SiGe heterostructure with the quantum well laying at the surface, revealing weak antilocalization. By fitting quantum correction to magneto-conductivity characteristic transport times and spin splitting energy of 2D holes are extracted. Additionally, suppression of weak antilocalization by a magnetic field parallel to the quantum well is reported and this effect is attributed

to surface roughness and virtual occupation of unoccupied subbands. Finally, chapter number six reports measurements of quantization of conductance in strained Ge/SiGe heterostructure with a buried quantum well. First the heterostructure is characterized by means of magneto-conductance measurements in a Hall bar device. Then another device engineered specifically as a quantum point contact is measured and displays steps of conductance. Magnetic field dependence of these steps is measured and an estimation of the g-factor for heavy holes in germanium is extracted.

# References


[1] Richard P. Feynman. Simulating physics with computers. *International Journal of Theoretical Physics*, 21(6):467–488, 1982.

[2] David P DiVincenzo et al. The physical implementation of quantum computation. *arXiv preprint quant-ph/0002077*, 2000.

[3] Daniel Loss and David P. DiVincenzo. Quantum computation with quantum dots. *Phys. Rev. A*, 57:120–126, Jan 1998.

[4] Sandra Foletti, Hendrik Bluhm, Diana Mahalu, Vladimir Umansky, and Amir Yacoby. Universal quantum control of two-electron spin quantum bits using dynamic nuclear polarization. *Nature Physics*, 5(12):903–908, 2009.

[5] S Nadj-Perge, SM Frolov, EPAM Bakkers, and Leo P Kouwenhoven. Spin-orbit qubit in a semiconductor nanowire. *Nature*, 468(7327):1084–1087, 2010.

[6] Simon J Devitt, William J Munro, and Kae Nemoto. Quantum error correction for beginners. *Reports on Progress in Physics*, 76(7):076001, 2013.

# Chapter 1

# Advantages of strained germanium for quantum spintronics

The prospect of a quantum computer implies the realization of tens of coherently coupled quantum bits or qubits [1]. While creating a single qubit can already be challenging, fault-tolerant quantum computation requires that the qubits used possess high fidelity [2]. Each individual qubits can have a different fidelity and while some of the parameters influencing this fidelity are dependent on the type of qubit realized and the measurement setup, the host material for the qubit plays a large role in the gate control fidelity and defines the upper bound limit of the qubit fidelity.

It is possible to define a quality factor $Q$ for a qubit representing its efficiency at gate control [3]. This quality factor $Q = T_2^{Rabi} / T_\pi$ represents the ratio between the qubit decay time $T_2^{Rabi}$ and the $\pi$ rotation time of the qubit quantum state. A higher $Q$ factor then represents a higher probability of the response to a qubit manipulation to be coherent with the initial state.

Choosing a good host material for spin qubits is then of the utmost importance as the nature of the material will have a big impact on the quality factor. On the $\pi$ rotation time first as the presence of spin orbit interaction can help the manipulation of the spin by fully electrical control. On the qubit decay time $T_2^{Rabi}$ then as the hyperfine interaction is the main reason for spin decoherence in quantum dots and is due to the presence of nuclear

spins in the host material. Germanium presents advantages in both parameters as will now be detailed.

## 1.1 Hyperfine interaction

When using the spin of an electron or a hole to encode quantum information, as in spin qubits, it is important that the spin maintains its phase for a duration long enough so that it can be manipulated or read and that the end state of this operation is coherent with the initial state. While in bulk semiconductors, charge carriers spin decoherence mainly occurs due to scattering through mechanism such as D'Yakonov-Perel [4], in quantum dots where charge carriers are confined, the main source of decoherence is the hyperfine interaction, that is to say the electron-nucleus spin interaction.

As opposed to an atom where the spin of an electron only interacts with the spin of its own nucleus through hyperfine coupling, in quantum dots, the spin of a charge carrier will interact with a lot of nuclei ($N \simeq 10^5$) and their spins (see Fig.:1.1a)[5]. The slow and random fluctuations of the effective magnetic field created by these nuclear spins (known as the Overhauser field) will in turn induce a random evolution of the charge carrier spin, thus inducing decoherence.

To the first order, the hyperfine interaction can be considered only as a Fermi contact hyperfine interaction whose Hamiltonian can be written as:

$$\mathscr{H} = \sum_{k}^{n} (A_k \vec{I}_k \vec{S}) \tag{1.1}$$

Where $\vec{I}_k$ is the spin operator for the nucleus $k$ and $\vec{S}$ the one for the charge carrier spin. The term $A_k$ represents the coupling strength between the nucleus spin $k$ and the carrier spin, and is proportional to the square of the overlap of the nucleus and carrier $k$ wavefunctions.

The first reason why strained Ge is so interesting as a host material for qubits with regards to hyperfine interaction comes from the nature of the charge carrier. While as of today most qubits experiments have been performed with electrons, intrinsic compres-

sively strained Ge, whether in core/shell nanowire or in two-dimensional heterostructures form holes quantum wells [6][7]. With regard to hyperfine interaction, the main advantage of holes as opposed to electrons comes from the overlap of their wavefunction with nuclei spin wavefunction. Electron conduction states are formed from atomic $s$ orbitals, meaning that the amplitude of their wavefunction is larger at the location of the nuclei. On the other hand, holes conduction states are formed from atomic $p$ orbital which amplitude is 0 at the location of the nuclei. This implies that the Fermi contact hyperfine interaction is equal to zero for conduction holes as the $A_k$ of the Hamiltonian are equal to zero.

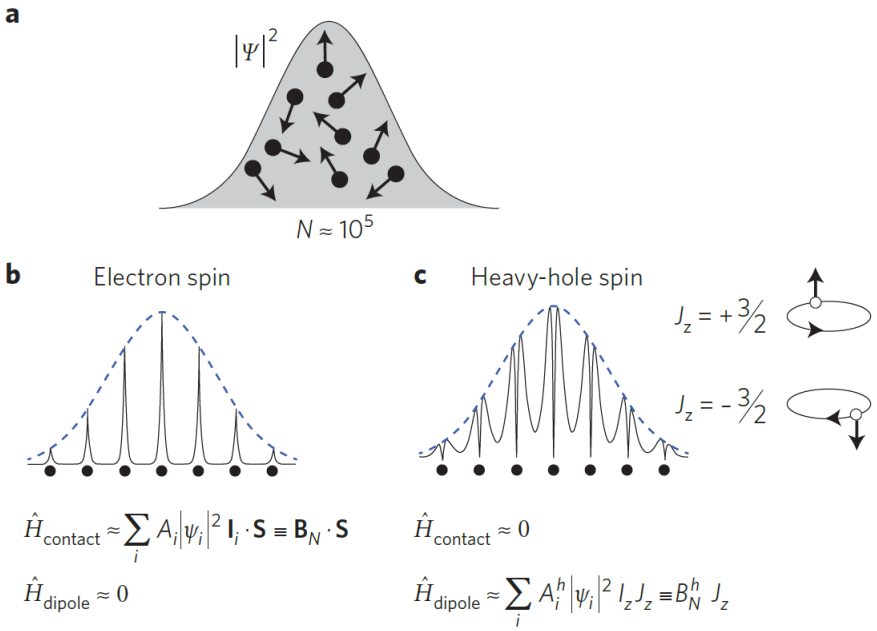


**Fig. 1.1: a:** The electron or hole wavefunction spatial extension covers around $N \simeq 10^5$ atoms, interacting with their spins. **b:**Electron conduction states are formed from atomic $s$ orbitals of which the amplitude is localized on a unit cell. **c:** Holes conduction states are formed from atomic $p$ orbital which amplitude is 0 at the location of the nuclei. From [5]

With holes as charge carriers, the only influence of the hyperfine interaction on the carrier spin is through a dipole-dipole interaction between the carrier and nucleus spins. Conduction electrons are formed from $s$ orbitals and dot not possess an angular momentum, thus they dot not have a dipole-dipole interaction with the nuclei spins. Conduction holes on the other hand are formed from $p$ orbitals and have a non-zero angular mo-

mentum. Pure heavy holes for example have $J_z = \pm 3/2$. This will induce a dipole-dipole interaction between the hole spin and the different nucleus spins. Still this interaction has been shown to be around 10 times weaker than the contact Fermi interaction of electrons [8], thus confirming that using holes as charge carriers is an advantage with regards to spin qubit coherence time.

When looking at the strength of the dipole-dipole interaction for holes or the Fermi contact interaction if electrons are used as charge carriers, germanium shows a second advantage over other standard spintronic materials and this advantage is related to the spin of the Ge nuclei. The only natural isotope of germanium with a non zero nuclear spin is $^{73}$Ge (spin equal to 9/2) and has a natural abundance of only 7.73%. Looking back at equation 1.1 for the Fermi contact interaction for electrons in Ge, one can understand that with most of the $\vec{I_k}$ equal to zero, the interaction will be weaker than for another material like GaAs where all isotopes of both elements have a non zero nuclear spin. Still, Ge is less attractive than Si in this regard as the only isotope with non zero nuclear spin is $^{29}$Si (spin equal to 1/2) and has a natural abundance of only 4.68%. The same principles apply for the dipole-dipole interaction, which will be weaker in Ge than in other III-V materials but still stronger than in Si due in part to natural abundance but mostly due to the fact that a spin 9/2 will create a much stronger dipole than a spin 1/2. A summary of natural isotopes of the most commonly used elements for spintronic and their respective spins is given in table 1.1.

## 1.2 Spin orbit interaction in quantum dots

Spin qubits use the spin of a charge carrier as a two level system to encode quantum information [9]. To engineer such a qubit, it is then required to be able to drive coherently the spin between these two levels. One possible technique is Electron Spin Resonance or ESR which uses an oscillating magnetic field to induce coherent rotations of the spin state. Still, this technique presents some drawbacks. It usually requires a microfabricated ESR antenna, i.e. a conducting line close to the qubit, through which an oscillating current is

| Element | Isotope | Spin | Natural abundance (% atom) |
|---|---|---|---|
| Germanium | $^{70}$Ge | 0 | 20.84 |
| | $^{72}$Ge | 0 | 27.54 |
| | $^{73}$Ge | 9/2 | 7.73 |
| | $^{74}$Ge | 0 | 36.28 |
| | $^{76}$Ge | 0 | 7.61 |
| Silicon | $^{28}$Si | 0 | 92.23 |
| | $^{29}$Si | 1/2 | 4.68 |
| | $^{30}$Si | 0 | 3.09 |
| Gallium | $^{69}$Ga | 3/2 | 60.10 |
| | $^{71}$Ga | 3/2 | 39.90 |
| Indium | $^{113}$In | 9/2 | 4.29 |
| | $^{115}$In | 9/2 | 95.71 |
| Arsenic | $^{75}$As | 3/2 | 100 |
| Antimony | $^{121}$Sb | 5/2 | 57.21 |
| | $^{123}$Sb | 7/2 | 42.79 |

**Table 1.1:** Natural isotopes, spin and natural abundance for most commonly used elements in spintronic

driven, thus generating an oscillating magnetic field. Due to Joule heating, this technique cannot allow for fast rotation of the spin, which in turns leads to low qubit fidelity.

In a sample where charge carriers experience spin orbit interaction, a second possibility arises. Indeed, spin orbit interaction, as will be detailed in chapter 3, links the spin of a particle to its orbital motion. In a quantum dot, due to the little amount of space available for the charge carriers to move in, one may expect spin orbit interaction to have a limited effect. While it is definitely different from the effect observed in bulk materials, the spin orbit interaction affects the spins of confined particles in a quantum dot by mixing the pure spin states $|\uparrow\rangle$ and $|\downarrow\rangle$. The eigenstates are then admixtures of spin and orbital degrees of freedom.

This is a significant change as an electric field cannot induce transitions between pure spin states, but it can for these mixed states. One can then produce an oscillating electric field on a quantum dot rather than a magnetic field and then drive the spin of a charge carrier from one state to the other. This spin control technique called Electrically Driven Spin Resonance or EDSR is far more efficient than ESR in terms of potential spin rotation time.

A strong spin orbit interaction can also have drawbacks for a qubit though. While it allows for faster qubit manipulation, thus shorter $T_\pi$, a strong mixing of the pure spin states $|\uparrow\rangle$ and $|\downarrow\rangle$ can make the system sensitive to charge fluctuation in its environment such as electrostatic gate noise, thereby leading to shorter decay time $T_2^{Rabi}$. This is why it is still relevant to perform research toward new materials for quantum spintronics, in order to find a material with the most effective balance between pros and cons. Germanium could be this material as it is known to show spin orbit interaction [10].

# References


[1] David P DiVincenzo et al. The physical implementation of quantum computation. *arXiv preprint quant-ph/0002077*, 2000.

[2] Emanuel Knill. Quantum computing with realistically noisy devices. *Nature*, 434(7029):39–44, 2005.

[3] Kenta Takeda, Jun Kamioka, Tomohiro Otsuka, Jun Yoneda, Takashi Nakajima, Matthieu R. Delbecq, Shinichi Amaha, Giles Allison, Tetsuo Kodera, Shunri Oda, and Seigo Tarucha. A fault-tolerant addressable spin qubit in a natural silicon quantum dot. *Science Advances*, 2(8), 2016.

[4] MI Dyakonov and VI Perel. Spin relaxation of conduction electrons in noncentrosymmetric semiconductors. *Soviet Physics Solid State, Ussr*, 13(12):3023–3026, 1972.

[5] Richard J Warburton. Single spins in self-assembled quantum dots. *Nature materials*, 12(6):483–493, 2013.

[6] Wei Lu, Jie Xiang, Brian P Timko, Yue Wu, and Charles M Lieber. One-dimensional hole gas in germanium/silicon nanowire heterostructures. *Proceedings of the National Academy of Sciences of the United States of America*, 102(29):10046–10051, 2005.

[7] Rai Moriya, Kentarou Sawano, Yusuke Hoshi, Satoru Masubuchi, Yasuhiro Shiraki, Andreas Wild, Christian Neumann, Gerhard Abstreiter, Dominique Bougeard, Takaaki Koga, and Tomoki Machida. Cubic rashba spin-orbit interaction of a two-dimensional

hole gas in a strained-ge/sige quantum well. *Physical review letters*, 113(8):086601, 2014.

[8] Christophe Testelin, Frédéric Bernardot, Benoît Eble, and Maria Chamarro. Hole–spin dephasing time associated with hyperfine interaction in quantum dots. *Physical Review B*, 79(19):195440, 2009.

[9] Daniel Loss and David P. DiVincenzo. Quantum computation with quantum dots. *Phys. Rev. A*, 57:120–126, Jan 1998.

[10] Christopher Morrison, Jamie Foronda, P Wiśniewski, SD Rhead, David R Leadley, and Maksym Myronov. Evidence of strong spin–orbit interaction in strained epitaxial germanium. *Thin Solid Films*, 602:84–89, 2016.

# Chapter 2

# Quantum dots and double dots systems

In electronic transport in semiconductors, one of the basic system that can be fabricated is a quantum dot. In these elements the quantification of charge plays a very important role in the transport characteristics, allowing them to be used as blocks of a more complex device to perform charge sensing, electronic thermometry or spin readout for example. In this section, the physics behind quantum dots and double dot systems as well as the experimental evidences of these properties in electronic transport are explained in the scope of the work performed in this thesis.

## 2.1 Quantum dots

### 2.1.1 Device geometry

In order to engineer a quantum dot for electronic transport, one has to isolate a small section of a bigger semiconductor system. This is usually done in nanowires or two-dimensional electron/hole gases as will be shown in this thesis or in semiconductor islands such as self assembled quantum dots [1]. Tunnel barriers are used for separation from the rest of the system in order to allow for charge transport across the dot as required for transport experiments. These barriers can be created by electrostatic gating [2] or by

materials interfaces [3]. The quantum dot is usually connected to one or several gates called plunger gates in order to modify the electrostatic potential of the dot [4].

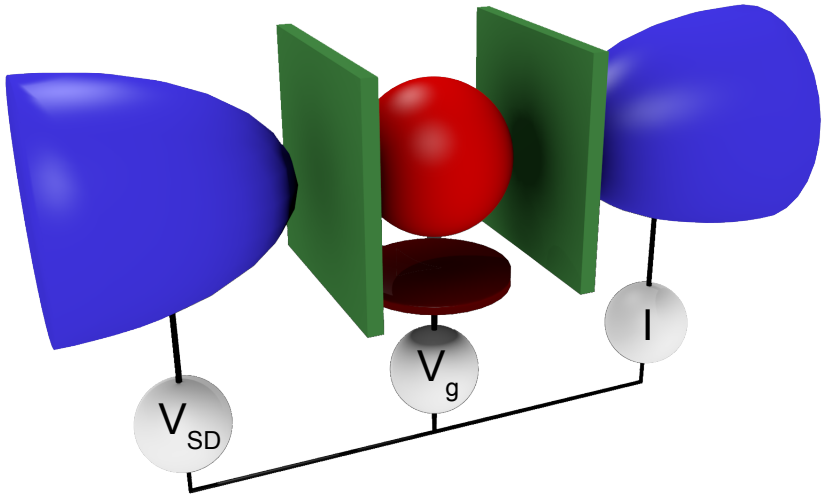


**Fig. 2.1:** Schematic of a quantum dot (red) connected to the rest of the system by leads (blue) through tunnel barriers (green). Transport experiment are usually done by applying voltage on the source ($V_{SD}$) and measuring the current (I) going through. The chemical potential of the dot can be changed by applying a voltage ($V_g$) on a plunger gate (maroon)

### 2.1.2 Charging energy

In a quantum dot such as the one described previously, adding an electron requires an additional energy, or charging energy [5]. This energy consists in two phenomena. The first one, which is not exclusive to quantum dots is the coulombian repulsion term [6]. Charge carriers, whether they are electrons or holes are charged particles. In a small island of a metal or semiconductor, they will repel each other. This is why adding another charge will require an additional energy to counter this repulsion. This term will be equal to $e^2/C$ where $C$ is the total capacitance of the island to its environment. This phenomenon is the one behind the functioning of single electron transistors (SET) [7].

The second phenomena is at the essence of a quantum dot. Such a system has to be small enough so that the charge carriers have a deBroglie wavelength of approximately the

same size as the dot, meaning the maximum dot size is dependent on the material used (through the effective mass of the charge carrier). This implies that the charge carriers occupy discrete quantum levels that have a discrete energy spectrum (properties for which they are sometimes referred to as artificial atoms) [8]. This discrete energy spectrum is the reason why adding a charge carrier to a dot requires a second additional energy (that we will refer to as orbital spacing). The smaller the dot and the number of charge carriers in it, the bigger this orbital spacing term.

### 2.1.3 Coulomb peaks

When connecting a quantum dot to two reservoirs via tunnel barriers, charge carriers will tunnel in the dot in order to minimize the energy of the system. When no bias is applied across the dot, the levels of the reservoirs are aligned. As tunneling through a tunnel barrier is only allowed when the end level is aligned with the starting level, charge transport across the dot is only possible when the first available state in the dot is aligned with the reservoirs. In this configuration both the states with N and N+1 charges in the dot are possible where N is the total number of charge in the dot. When modifying the voltage applied on the plunger gate by $\Delta V_g$, the potential of the dot is changed by $\Delta\mu_{dot} = \alpha_g \times \Delta V_g$ where $\alpha_g$ is the lever arm of the gate on the dot ($\alpha_g = C_g/C$ where $C_g$ is the capacitance of the plunger gate to the dot). By linearly sweeping the plunger gate, one can switch the quantum dot from off to on for discrete values of $V_g$, when a level of the dot aligns with the leads. Probing the dot conductivity as a function of gate voltage will result in series of peaks called Coulomb peaks. In between these peaks, the system is blocked and the number of charge inside the dot is perfectly defined.[5]

As the Coulomb peaks appear when a dot level is aligned with the reservoirs Fermi energy, it is possible to extract the charging energy of the dot from the peak spacing via the formula $\Delta E_{N\rightarrow N+1} = \alpha_g \times \Delta V_{g,N\rightarrow N+1}$. When the dot is filled with a high number of charges, the coulombian repulsion term in the charging energy ($e^2/C$ where $C$ is the total capacitance of the dot to its environment) is dominant compared to the orbital

spacing of the dot. That leads to Coulomb peaks with highly regular spacing equal to $\Delta V_g = \Delta E/\alpha_g = e^2/\alpha_g C$ (see fig. 2.2).

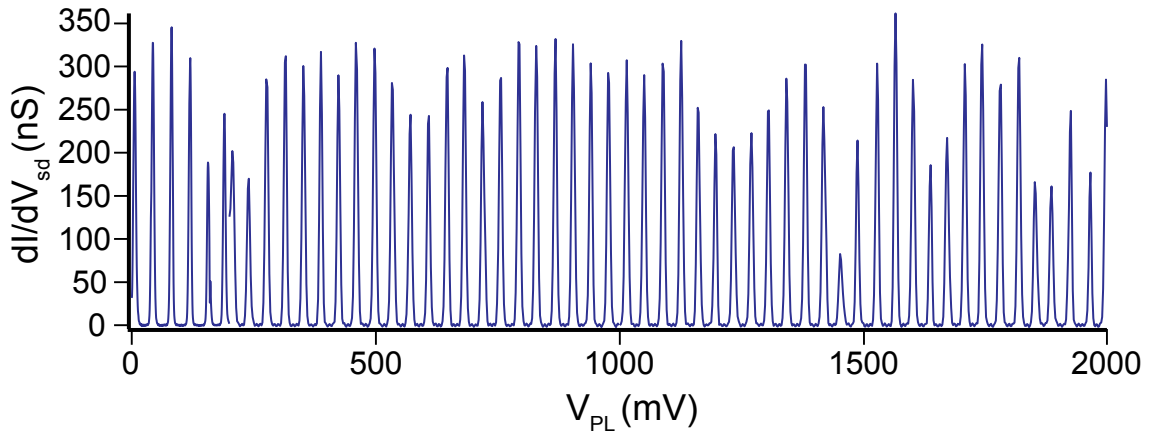


**Fig. 2.2:** A series of highly regularly spaced Coulomb peaks. Data from chapter 4

When the number of charges in the dot becomes smaller, the orbital spacing of the dot levels reaches the same order of magnitude as the coulombian repulsion energy, creating a difference between odd and even filling of the dot. When the dot is filled with an odd number of charges, adding one more will only require the coulombian energy as the new charge will occupy an orbital level already containing the previous charge. On the other hand, when adding a charge to a dot filled with an even number of charges, the required energy will be the coulombian term plus the orbital energy spacing between the last orbital level filled and the one the new charge will occupy.

When reaching the last few charges in a dot, the charging energy tends to increase a lot from one transition to the other. This is mainly due to two mechanisms. The first one is that the orbital spacing will continue increasing as the number of charges gets smaller, thus increasing the charging energy. The second reason is due to the fact that when reaching a low number of charges by the use of a gate, the electrical field created by the plunger will also modify the shape of the dot. This will lead to a modification of $C$ the total capacitance of the dot and of the gate lever arm $\alpha_g$, leading to a change in the coulombian repulsion energy. For these reasons, when trying to extract the charging

energy of a dot with a low number of charge, one has to perform bias spectroscopy of the dot.

### 2.1.4 Coulomb diamonds

When applying a voltage $V_{SD}$ between source and drain, an energy difference $qV_{SD}$ will be created between the two reservoirs. From now on we will consider that the charge carriers are holes, meaning that $q$ is equal to $e$ and not $-e$ as it would be for electrons. It means that in our case, for a positive bias, the holes in the source lead are of higher energy than the ones in the drain lead.

While with no bias applied the dot was in an on state only when a level was aligned with both contacts, it is now on whenever a level gets an energy situated in between the Fermi energies of the leads. When looking at the conductance of the dot as a function of gate voltage, what were previously peaks will then widen linearly and become plateaus as a function of bias as $w = \alpha_g V_{SD}$ where w is the plateau width. Measuring the current going through a quantum dot as a function of both gate voltage and bias will display distinctive features called Coulomb diamonds as the off region of the dot gets smaller as the bias gets higher (see fig. 2.3

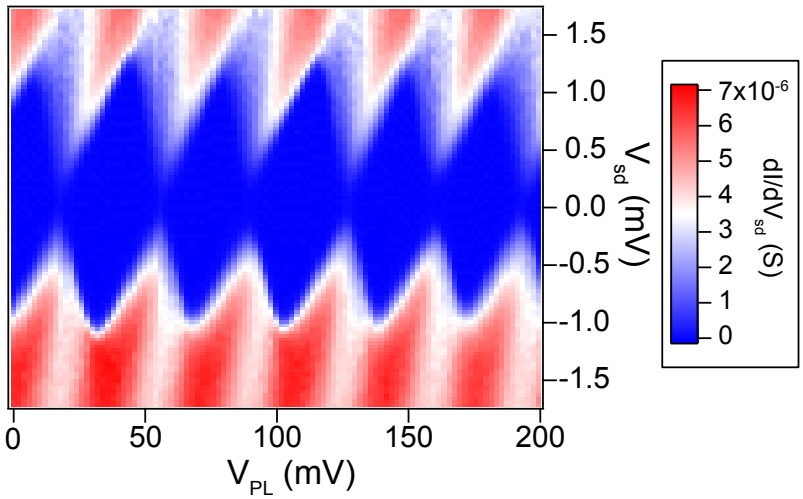


**Fig. 2.3:** Conductance of a dot as a function of bias and gate voltage. Data from chapter 4

With high enough bias, the dot will be in an on configuration for all gate voltage values. This happens when the bias window is big enough so that it becomes higher than the splitting between two levels of the dot, thus ensuring that at least one level will always be in the bias window regardless of the gate voltage. It allows for charging energy extraction from the Coulomb diamonds as the tip of a diamond represents the exact bias for which two dot levels enter the bias window, that is to say that $eV_{SD}$ is equal to the charging energy to go from one of these levels to the other.

## 2.2 Double dot systems

In order to perform a spin qubit, one has to readout the quantum state of the spin of a single charge carrier. The magnetic moment of a single spin being so weak, it is extremely difficult to perform its electrical readout directly [9]. To counter this difficulty, it is possible to conceive charge transport processes that are spin selective, that is to say to perform spin to charge conversion. It is then easier to measure charge than spin. The most common process used relies on Pauli spin blockade and requires two quantum dots in series, a system whose physics will now be detailed.

### 2.2.1 Stability diagram

The stability diagram of a double dot system represents the charge configuration of the dots as a function of both gates voltage. The experimental depiction of this diagram is the measurement of the conductivity of the double dot system as a function of gates voltage. For a system made of two quantum dots in series to be conductive, both of the dots must be in an on state at the same time. A simplistic representation of this would be to first consider both dots independently with their own conductance resonances, and just consider that the system will be conducting when both gate voltages will attain the values of resonance, as depicted on fig 2.4 a.

This picture is only true for completely decoupled quantum dots. When the two dots are close enough, there is a cross capacitance of the gates, meaning that varying the gate

voltage of one dot will also vary the energy levels of the other dot. This implies that the voltages at which each dot gets its resonances will not be constant but will vary linearly with the gate voltage of the other dot, as shown in fig 2.4 b.

The most important difference between this first approach to a stability diagram and the reality of coupled quantum dots is the separation of the resonances. Each of the resonances depicted before are actually split into two resonances in a coupled double dot system and the diamond shaped regions where charge configurations are defined turn into hexagons (see fig 2.4 c). This has to be explained by a charging energy of the whole system. Resonances are points in the stability diagram where several charge configuration are favorable, thus allowing charges to go across the system. Splitting of the resonances in a coupled double dot system is the evidence that is not possible to go straight from a $(N_1,N_2)$ charge configuration to a $(N_1+1,N_2+1)$ (where $N_i$ is the charge number in the dot i). One could imagine that such a change in charge configuration would be possible if both the dots and contacts levels were aligned, but then adding a charge to one of the two dots would lift the level of the second one, due to the cross capacitance. Additional gate voltage would then be required for a charge to enter the second dot.

Each of the resonances is then a gate configuration where three charge configurations of the charge system are accessible, explaining why they are sometimes referred to as triple points. This allows for charge transfer across the system through a cycle of the type $(N_1,N_2)\rightarrow(N_1+1,N_2)\rightarrow(N_1,N_2+1)\rightarrow(N_1,N_2)$ or $(N_1,N_2+1)\rightarrow(N_1+1,N_2+1)\rightarrow(N_1+1,N_2)\rightarrow(N_1,N_2+1)$, thus making the double dot system conducting.

While technically challenging [10], for spin qubit engineering, it is usually useful to use the stability diagram to set the system on the triple point with the lowest number of charges. While the physics behind quantum dot levels and spin and charges interaction is well understood for few charges systems, systems with higher number of charges can be hard to describe and tune precisely [11].

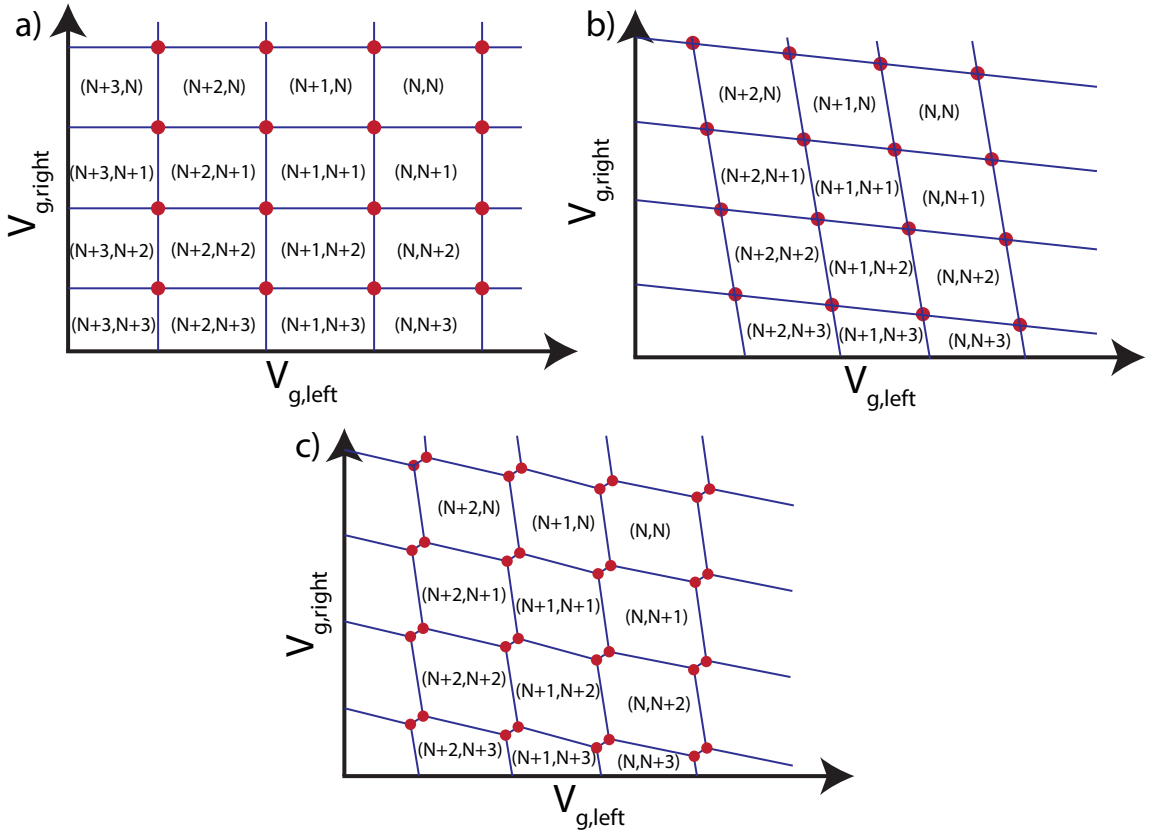


**Fig. 2.4:** Schematic of the stability diagram of a double dot system. a) Case with no coupling between the two dots. b) Cross capacitance of the plungers of the two dots is now taken into account. c) Coupling between the two dots splits each resonance into two triple points

### 2.2.2 Conductance resonances characteristics

In the previous section, no bias was considered across the system. Since source and drain Fermi levels are aligned, resonances only appear for discrete values of gate voltages. When bias is applied between source and drain, it opens windows of conductance. The formerly point-like resonances will then turn into triangles.

As the bias is increased, the triangles get bigger. With high enough bias, there will be gate voltage values for which not only the ground state of a dot level is in the bias window but also one or more excited state. This will increase the conductance of the system as more levels are available for tunneling. In a conductance triangle, the position of the increase of conductance allows for excited states energy reading [12].

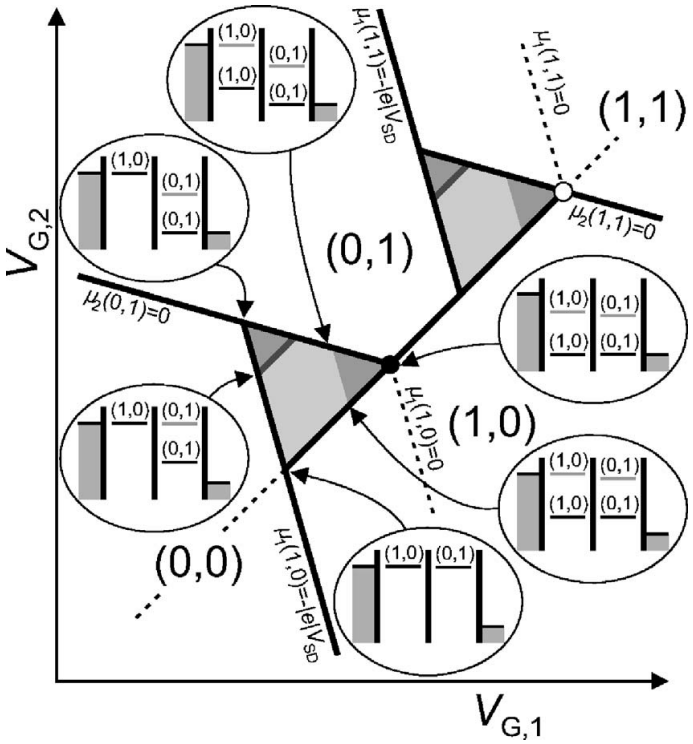


**Fig. 2.5:** Schematic of a double triangle resonance (for an electron double dot), showing the dots levels configuration for each features of the triangles. From [13].

### 2.2.3 Pauli spin blockade

Until now, only spinless charge carriers were considered, but holes and electrons have a spin 3/2 and 1/2 respectively, leading to interesting phenomena on conduction in the presence of magnetic field due to Pauli exclusion principle. Let us now consider for example the charge triple point where transport through the double dot is done through the cycle (0,1)→(1,1)→(0,2)→(0,1). Let us also consider an external magnetic field applied on the system. This will lift the degeneracy between the spin up ($|\uparrow\rangle$) and spin down ($|\downarrow\rangle$) states of the dots.

Considering the transport cycle mentioned earlier, a hole will first enter the left dot. There is no selection of the hole leaving the lead with regard to its spin as it enters the dot on a new orbital. It will then try to tunnel to the right dot on an orbital where a hole is already present, leading to two possible scenarios. Either the hole on the left dot has its spin opposite to the one of the hole in the right dot. It will then be allowed to tunnel to

the right dot as they will form a spin singlet and will continue the cycle. Either the hole as the same spin direction as the one in the right dot. It will then not be allowed to tunnel to the right where it should form a spin triplet on the orbital which is not permitted due to Pauli exclusion principle. The hole will not be able to go back to the lead either as it has an energy lower that the Fermi level of the lead. Transport is then blocked in the system. This phenomena is called Pauli spin blockade.

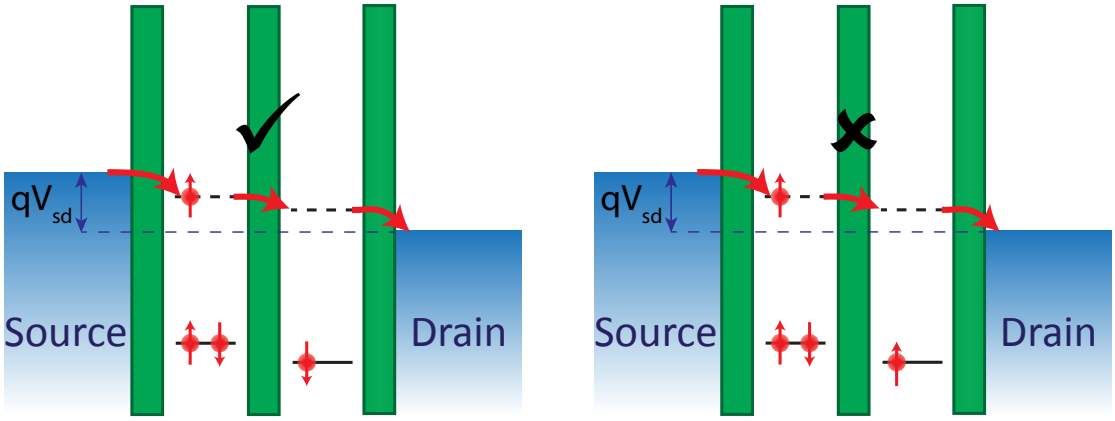


**Fig. 2.6:** Schematic representing the conditions in which spin selectivity in a double dot system can induce suppression of current. This phenomena is called Pauli spin blockade.

If the bias is reversed, then Pauli spin blockade is suppressed. Indeed, the conduction cycle of the holes becomes (0,1)→(0,2)→(1,1)→(0,1). Here, blockade doesn't happen as there will always be a hole in the right lead with the correct spin direction to enter the right dot. Any of the two holes in the right dot will then be able to tunnel to the left dot and then to the left lead, thus restarting the cycle.

Not all triple points meet the conditions to observe Pauli spin blockade. For example the triple point for which conduction involves the cycle (0,1)→(1,1)→(1,0)→(0,1) will not have spin blockade as it does not involve spin selectivity. Spin selectivity only occur when the cycle involves a transition $(N_1+1,N_2+1)\rightarrow(N_1,N_2+2)$ or $(N_1+1,N_2+1)\rightarrow(N_1+2,N_2)$ where $N_1$ and $N_2$ are even numbers of charge. It can be shown that this spin selectivity can occur for only one fourth of the triple points for a given bias direction and for another fourth of

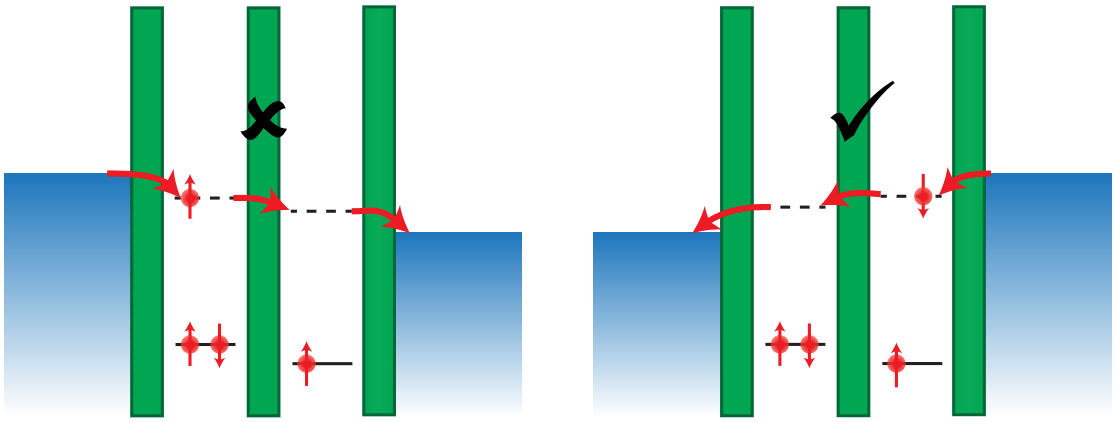

**Fig. 2.7:** Schematic for two opposing biases of a double sot system. Pauli spin blockade appears for positive bias, but disappear when the bias is reversed.

the triple points for the opposite bias direction. It is also to be noted that the Pauli spin blockade conditions for a bias direction are met for both triple points of a pair of triangles if they are met for one of them.

Experimentally, when Pauli spin blockade occurs, triangle resonances are usually not fully suppressed. It can happen that some edges of the pair of triangles are still visible. It represents the configuration when the level of the first dot is aligned with the Fermi level. There, when a hole with the wrong spin enters the first dot, it will not be able to tunnel through the system, but can go back to the lead. This cycle will happen until a hole with the right spin enters the dot and tunnels through the system (see fig 2.8 a). Another possibility is that only a region at the base of the triangles disappears due to Pauli spin blockade. This happens when the bias applied is high enough so that the triplet state of the (0,2) configuration becomes available for transport through the system. When magnetic field is applied, current is suppressed over the region (adjacent to the base) where tunneling can only occur through the singlet of (0,2), the triplet state of (0,2) being energetically inaccessible (see fig 2.8 b).

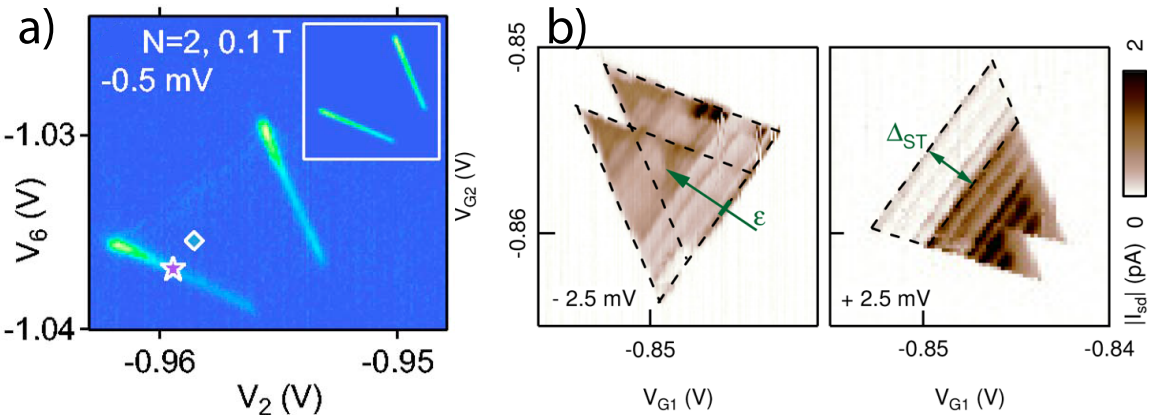


**Fig. 2.8:** Experimental evidences of Pauli spin blockade. **a)** Only the edges of the pair of triangle still conduct (from [14]). **b)** Current is suppressed in a region near the base of the triangles. The extension of this spin blockaded region measured along the level detuning direction (perpendicular to the base) is set by the energy splitting $\Delta_{ST}$ between singlet and triplet in the (0,2) charge configuration (from [15])

# References


[1] N Ares, G Katsaros, VN Golovach, JJ Zhang, A Prager, LI Glazman, OG Schmidt, and S De Franceschi. Sige quantum dots for fast hole spin rabi oscillations. *Applied Physics Letters*, 103(26):263113, 2013.

[2] Carina Fasth, Andreas Fuhrer, Mikael T Björk, and Lars Samuelson. Tunable double quantum dots in inas nanowires defined by local gate electrodes. *Nano letters*, 5(7):1487–1490, 2005.

[3] Mikael T. Björk, Claes Thelander, Adam E. Hansen, Linus E. Jensen, Magnus W. Larsson, L. Reine Wallenberg, and Lars Samuelson. Few-electron quantum dots in nanowires. *Nano Letters*, 4(9):1621–1625, 2004.

[4] J. R. Petta, A. C. Johnson, J. M. Taylor, E. A. Laird, A. Yacoby, M. D. Lukin, C. M. Marcus, M. P. Hanson, and A. C. Gossard. Coherent manipulation of coupled electron spins in semiconductor quantum dots. *Science*, 309(5744):2180–2184, 2005.

[5] Leo P Kouwenhoven, Charles M Marcus, Paul L McEuen, Seigo Tarucha, Robert M Westervelt, and Ned S Wingreen. Electron transport in quantum dots. In *Mesoscopic electron transport*, pages 105–214. Springer, 1997.

[6] HR Zeller and I Giaever. Tunneling, zero-bias anomalies, and small superconductors. *Physical Review*, 181(2):789, 1969.

[7] Marc A Kastner. The single-electron transistor. *Reviews of Modern Physics*, 64(3):849, 1992.

[8] RC Ashoori, HL Stormer, JS Weiner, LN Pfeiffer, SJ Pearton, KW Baldwin, and KW West. Single-electron capacitance spectroscopy of discrete quantum levels. *Physical review letters*, 68(20):3088, 1992.

[9] JM Elzerman, R Hanson, LH Willems Van Beveren, B Witkamp, LMK Vandersypen, and Leo P Kouwenhoven. Single-shot read-out of an individual electron spin in a quantum dot. *nature*, 430(6998):431–435, 2004.

[10] J. M. Elzerman, R. Hanson, J. S. Greidanus, L. H. Willems van Beveren, S. De Franceschi, L. M. K. Vandersypen, S. Tarucha, and L. P. Kouwenhoven. Few-electron quantum dot circuit with integrated charge read out. *Phys. Rev. B*, 67:161308, Apr 2003.

[11] R. C. Ashoori, H. L. Stormer, J. S. Weiner, L. N. Pfeiffer, K. W. Baldwin, and K. W. West. N. *Phys. Rev. Lett.*, 71:613–616, Jul 1993.

[12] W. G. van der Wiel, S. De Franceschi, J. M. Elzerman, T. Fujisawa, S. Tarucha, and L. P. Kouwenhoven. Electron transport through double quantum dots. *Rev. Mod. Phys.*, 75:1–22, Dec 2002.

[13] R Hanson, LP Kouwenhoven, JR Petta, Seigo Tarucha, and LMK Vandersypen. Spins in few-electron quantum dots. *Reviews of Modern Physics*, 79(4):1217, 2007.

[14] A. C. Johnson, J. R. Petta, C. M. Marcus, M. P. Hanson, and A. C. Gossard. Singlet-triplet spin blockade and charge sensing in a few-electron double quantum dot. *Phys. Rev. B*, 72:165308, Oct 2005.

[15] Ruoyu Li, Fay E. Hudson, Andrew S. Dzurak, and Alexander R. Hamilton. Pauli spin blockade of heavy holes in a silicon double quantum dot. *Nano Letters*, 15(11):7314–7318, 2015. PMID: 26434407.

# Chapter 3

# Spin orbit interaction

The spin orbit interaction (SOI) is one of the reasons why germanium is an interesting material for spintronic. In this chapter the physics of this interaction will be detailed, from its nuclear origin to the ability it provides to control electrically the spin of a charge carrier in a quantum dot.

## 3.1 Origin of spin orbit interaction

The SOI represents the coupling between the spin of an electron and its motion (its momentum), and can be treated as the effect of an effective $\vec{k}$-dependent magnetic field. For proper treatment of the SOI, one has to derive the Dirac equation, but it is possible to describe it as a relativistic correction to the Schrödinger equation as will now be done here.

A moving electron, orbiting around its nucleus or diffusing in a lattice, is a charged particle moving in an electric field. We can consider it as a reference frame (the electron rest frame) moving at a speed $\vec{v}$ relative to an electric field $\vec{E}$. Following classical electrodynamics, this will induce an effective magnetic field in the electron rest frame that can be written as:

$$\vec{B} = -\frac{1}{c}\vec{v} \times \vec{E} = \frac{1}{mc}(\vec{E} \times \vec{p}) \tag{3.1}$$

The electron, due to its magnetic moment $\vec{\mu}$, will then acquire an energy:

$$-\vec{\mu}.\vec{B} = -\gamma\vec{s}.\vec{B} = -\frac{\gamma}{mc}\vec{s}.(\vec{E}\times\vec{p}) \tag{3.2}$$

Where $\gamma$ is the gyromagnetic ratio and $\vec{s}$ the electron spin. Due to our assumption on the spin orbit (SO) term as a relativistic correction, this term is not fully correct and a full relativistic calculation would reveal a $1/2$ pre-factor known as Thomas factor [1].

As can be seen from formula 3.2, an electron in an electric field will acquire an energy linked to its spin and its momentum. It can also be seen that this energy is dependent on the form of the electric field, whether it is the field created by the nucleus around which the electron orbits, the field created by the crystal in which the electron travels, the asymmetry of the lattice cell or the asymmetry of the confinement potential. For these reasons, SOI can have quite different consequences depending on the system studied. The effects of SOI for our system of choice will now be detailed.

## 3.2 Spin orbit interaction effect on band diagram

Here we will now describe the consequences of SOI for our specific system, that is to say a two-dimensional hole gas (2DHG) in a germanium heterostructure. The effects of SOI in the case of a Ge/Si core/shell nanowire will not be detailed here as SOI had little to none influence on the experiments on this system described in this thesis. Still, a full derivation of SOI in this system can be found in a paper by Kloeffel et al. [2].

The first effect of SOI on our system of interest comes from the atomic SOI. Indeed, in an atom, negatively charged electrons orbit around their nucleus. But in the rest frame of the electron, the nucleus is a positive charge orbiting the electron. This will induce an electric field highly influenced from the orbit of the electron (SOI takes its name from this specific consideration). Specifically, it is possible to show that the SO energy is linked to the product $s.l$ where $s$ is the spin of the electron and $l$ its orbital momentum. This is of significant importance for our system, because in an electronic system, in a tight binding approach, electrons are described by s-like orbitals, for which the orbital momentum $l$

is equal to zero. Holes on the other hand are described by p-like orbitals, that is to say $l = 1$. Their total angular momentum $j$ can then have two different values, $j = 3/2$ and $j = 1/2$. In this situation, it can be shown that the atomic SOI will split these two subbands by an energy gap $\Delta_0$ called the spin orbit gap. In germanium, the spin orbit gap has been measured and a value of $\Delta_0 = 0.29$ eV has been obtained [3]. The $j = 1/2$ subband, of lower energy than the $j = 3/2$ one, is usually called the split-off band.

Additionally, it can be shown that the $j = 3/2$ subband splits again for a non zero wavevector $k$ into two subbands. Indeed when the quantization axis of the angular momentum $\vec{j}$ is chosen parallel to $\vec{k}$, SOI interaction will induce a $k$ dependent splitting between the $m = \pm 3/2$ states (called Heavy Hole states HH) and the $m = \pm 1/2$ states (Light Hole states LH) (see Fig.3.1).

Finally, in a two dimensional system, confinement will have an additional effect on the energy band diagram. Indeed, the projection of the electronic states in a 2DHG on the direction perpendicular to the quantum well (QW) corresponds to standing waves. This implies that even for an in-plane wave vector $k_{//}$ equal to zero, the total wave vector $k$ is not zero, leading to a splitting of the HH and LH states even at $k_{//} = 0$. This is for this reason that for low enough carrier densities, as it is the case in the experiments described in the next chapters, only the HH subband is occupied.

## 3.3 Rashba spin orbit interaction

Spin orbit interaction can also lift the spin degeneracy of subbands when the charge carrier travels in a solid with spatial inversion asymmetry. In two-dimensional systems, it exists two main phenomena that can break space reversal symmetry. The first one is known as bulk inversion asymmetry (BIA) and is responsible for Dresselhaus SO. This is of little interest for us as BIA is a consequence of the absence of inversion center in the crystal structure, which is not the case for germanium (BIA is particularly relevant for III-V materials such as GaAs). The Dresselhaus Hamiltonian $\mathscr{H}_D$ contains both a $k$-linear and $k$-cubic terms but the $k$-cubic terms are usually neglected due to their small contribution

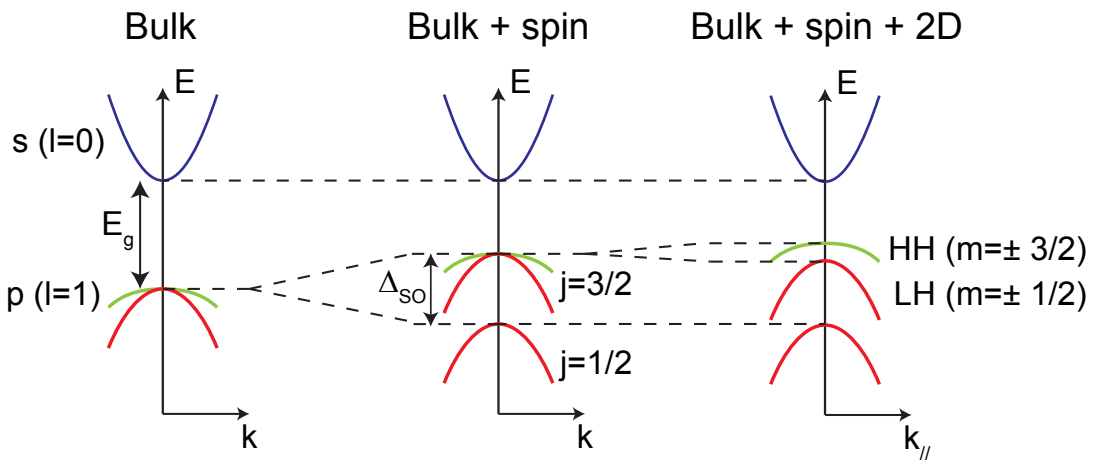


**Fig. 3.1:** ***left:*** Schematic of the energy band diagram for a bulk semiconductor. The valence and conduction bands are separated by the band gap $E_g$. The electrons are described by s-like orbitals ($l = 0$) while the holes are described by p-like orbitals ($l = 1$) ***center:*** Now taking into account spin, the SOI splits the valence band between the $j = 3/2$ states and the $j = 1/2$ states by a spin orbit gap $\Delta_0$ ***right:*** In a 2DHG, quantization in a direction perpendicular to the QW plane leads to a splitting of the HH and LH states, even at $k_{//} = 0$. Inspired from Winkler et al. and Moriya et al. [4, 5]

compared to the $k$-linear ones. Considering a basis $x$, $y$ and $z$ pointing along the main crystallographic direction (100), (010) and (001) respectively, and a 2D quantum well perpendicular to the (001) direction, this Dresselhaus Hamiltonian can be written as [6]:

$$\mathscr{H}_D = \beta\left[-k_x\sigma_x + k_y\sigma_y\right] \tag{3.3}$$

where $\beta$ is a pre-factor depending on material and confinement and $\sigma_i$ represents the Pauli matrices. It is often interesting to write this Hamiltonian as a Zeeman term $\mathscr{H}_D = \frac{1}{2}\vec{B}_D(\vec{k}_{//})\cdot\vec{\sigma}$, with $\vec{B}_D(\vec{k}_{//}) = 2\beta(-k_x, k_y)$. The direction of the effective field $\vec{B}_D$ created by the Dresselhaus SOI is represented in Fig.3.2a.

The second phenomena breaking space reversal symmetry is the structural inversion asymmetry (SIA) and is responsible for Rashba SO [7]. This type of SOI is the one to consider for a germanium 2DHG as it can be caused by an asymmetry of the confinement

or by an electric field perpendicular to the 2DHG. The Rashba SOI has seen extended studies in 2D electrons systems for which the Hamiltonian $\mathscr{H}_R$ can be given as:

$$\mathscr{H}_R = \alpha E_z i \left[k_- \sigma_+ - k_+ \sigma_-\right] \tag{3.4}$$

where $\alpha$ is a pre-factor depending on material, $E_z$ is the electric field perpendicular to the QW plane and we can define $k_+$, $k_-$, $\sigma_+$ and $\sigma_-$ as $k_\pm = k_x \pm i k_y$ and $\sigma_\pm = \frac{1}{2}(\sigma_x \pm i\sigma_y)$. Similarly to Dresselhaus SOI, the Rashba SOI can be written as a Zeeman term with the $k_{//}$-dependent effective field $\vec{B}_R(\vec{k}_{//}) = 2\alpha E_z(k_y, -k_x)$ (see Fig.3.2b). As can be seen from equation 3.4, Rashba SOI has the experimental advantage of being easily tuned by changing the electric field applied on the system.

For heavy holes systems, this Hamiltonian is not valid. Indeed, due to the effective spin 3/2 of HH, Pauli matrices $\sigma_x$ and $\sigma_y$ have to be replaced by $J_x$ and $J_y$, the 4 x 4 matrices corresponding to $j = 3/2$ [4]. This leads to a $k$-cubic dependence of the Hamiltonian in the form:

$$\mathscr{H}_{R^3} = \alpha_3 E_z i \left[k_+^3 \sigma_- - k_-^3 \sigma_+\right] \tag{3.5}$$

One of the major differences between cubic and linear Rashba SOI, beside the $k$-dependence, is in the parameters influencing the value of the $\alpha$ pre-factor. While the $\alpha$ pre-factor for linear Rashba SOI only depends on materials parameters, the $\alpha_3$ pre-factor for cubic Rashba SOI not only depends on material parameters but also on the QW geometry. This leads to a much more complex dependence of the SO energy with respect to electric field $E_z$. The effective field for cubic Rashba SOI is given by $\vec{B}_{R^3}(\vec{k}_{//}) = 2\alpha_3 E_z(k_y[k_y^2 - 3k_x^2], k_x[k_x^2 - 3k_y^2])$ (see Fig.3.2c).

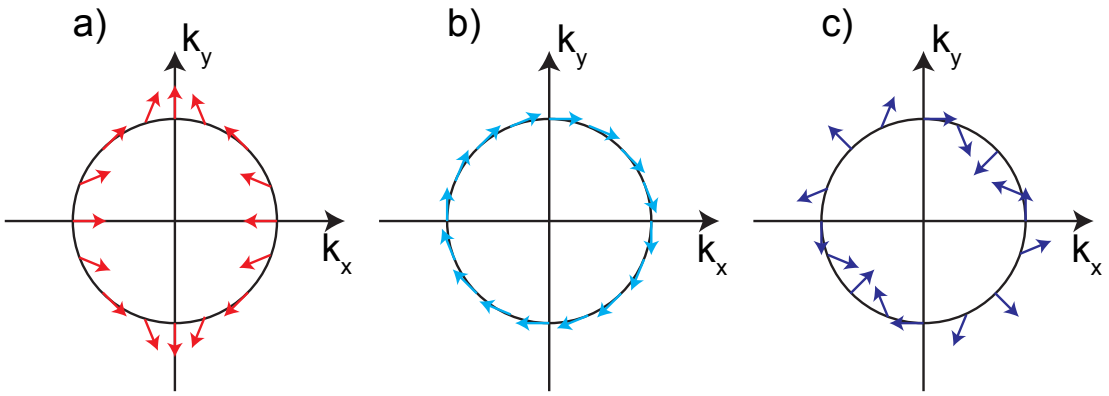


**Fig. 3.2:** Schematic representing the direction of the effective field of SO (colored arrows) as a function of the in plane wave vector for Dresselhaus SO (a), linear Rashba SO (b) and cubic Rashba SO(c)

## 3.4 Spin relaxation mechanisms

The spin of an electron is not fixed in time, as its direction can vary. This phenomena is called spin relaxation. Several mechanisms can explain spin relaxation of which the two prominent ones for 2DHG will now be explained.

### 3.4.1 Elliott-Yafet spin relaxation mechanism

The first mechanism is the Elliott-Yafet mechanism [8, 9]. Mostly happening in metals and small gap semiconductors, Elliot-Yafet mechanism explains spin relaxation by scattering-induced spin flips. During each scattering event of the charge carrier, its spin will rotate randomly by an infinitesimally small angle. The succession of scattering events will induce a randomization of the spin with regards to its initial value. For this reason, Elliott-Yafet mechanism is characterized by a spin relaxation time $\tau_{SO}$ (the average time of travel after which the spin has performed a $\pi$-rotation) proportional to the scattering time $\tau_{tr}$ (the average time between two scattering events).

### 3.4.2 D'Yakonov-Perel spin relaxation mechanism

The second mechanism and the one of interest in the case of germanium 2DHG is the D'Yakonov-Perel mechanism [10]. As seen previously, a hole traveling in a solid lacking inversion symmetry will experience an internal magnetic field, the SO field. The spin of the hole will then precess around this internal field. But at each scattering event, the momentum of the hole will shift and so will do the internal field. As the hole goes through a succession of scattering events, its spin will go through a succession of precession around random axes, then losing memory of its initial state.

As opposed to Elliot-Yafet mechanism, in the case of D'Yakonov-Perel spin relaxation mechanism, the spin relaxation time $\tau_{SO}$ is inversely proportional to the scattering time $\tau_{tr}$. This can be explained by the fact that if the time in between scattering events is too short (small $\tau_{tr}$), the spin of the charge carrier will not have enough time to rotate significantly, thus giving a long spin relaxation time $\tau_{SO}$.

## 3.5 Weak antilocalization theory

In order to study the strength of the spin-orbit interaction in a two dimensional material, it is possible to look for evidence of weak antilocalization. This phenomenon tends to increase conductivity in a low dimensional system with strong spin-orbit interaction, at low temperature, by reducing the back scattering probability of charge carriers. In order to better understand it, we will first explain the theory behind weak localization, the no spin-orbit counterpart of weak antilocalization that reduces the conductivity of a system. We will then explain how spin orbit interaction reverses this effect.

### 3.5.1 Weak localization

The diffusive motion of charge carriers in disordered systems such as semiconductors is well explained by the Drüde model. At low temperature, this model is still viable for large samples (where transport is diffusive) but corrections need to be made to take into account the quantum properties of transport.

When considering a pair of trajectories between two points of a diffusive sample, of amplitudes $A_1$ and $A_2$, the Drüde model adds them classically, leading to a global amplitudes of the two paths $A$ that is:

$$|A|^2 = |A_1|^2 + |A_2|^2 \tag{3.6}$$

But at low temperature where quantum properties have to be taken into account, we now have to consider the full quantum amplitude including the phase for each path. We then have:

$$|A|^2 = |A_1|^2 + |A_2|^2 + 2|A_1 A_2|\cos\theta \tag{3.7}$$

where $\theta$ is the phase difference between the two paths. The additional term $2|A_1 A_2|\cos\theta$ represents the interference term of the two paths.

On average over all paths and due to disorder, this cosine of phase difference averages to 0 ($\langle\cos\theta\rangle = 0$) except for a certain class of loops being the self intersecting paths. For these trajectories, the charge carrier can go around a loop in both directions, meaning these trajectories are representative of two paths that can interfere.

It is possible to show that the interference of the two paths will be constructive only when the charge carrier is backscattered. Calculations behind this assertion will not be given here [11] but one simple explanation is that in order for a charge carrier to accumulate the same phase in one direction of the loop or the other, it has to go through the same momentum shifts at the scattering centers creating the trajectories. This is only possible if the end wavevector of the loop trajectory $\vec{k}'$ is equal to $-\vec{k}$ where $\vec{k}$ is the initial wavevector (see Fig. 3.3). As the two paths have the same amplitude ($A_1 = A_2$) and their phase difference is equal to zero ($\cos\theta = 1$), we have $|A|^2 = 4|A_1|^2$. This results means that in these loops, the probability for a charge carrier to be back scattered is twice as high ($4|A_1|^2$) as it would be without taking interferences into account ($2|A_1|^2$).

Since all these self intersecting paths in the sample will tend to enhance the global backscattering of charge carriers, they will have a negative contribution to the conductivity

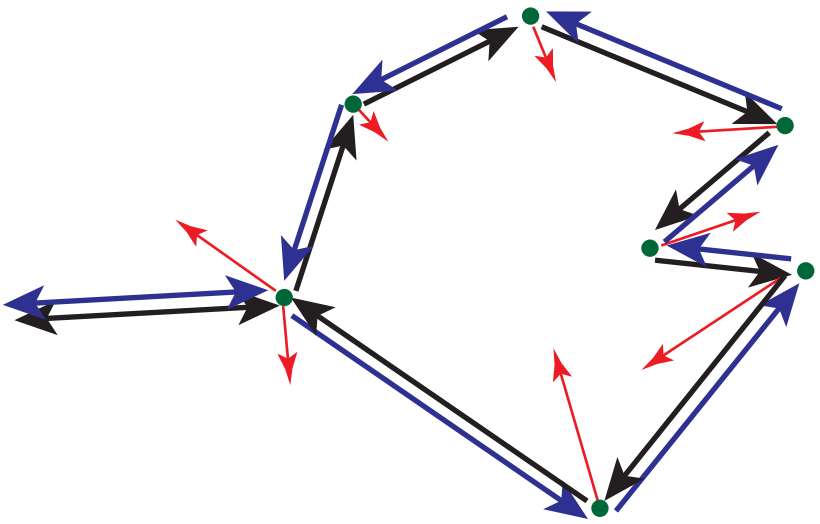

**Fig. 3.3:** Example of a self intersecting path inducing weak localization. When going clockwise (black path) or counter clockwise (blue path) the charge carrier will experience the same momentum shifts (red arrows) on scattering centers (green dots) (thus getting the same phase accumulation) only when being back scattered.

of the sample over the classical Drüde conductivity. This is the phenomenon called weak localization.

Weak localization effect is only observable due to the magnetic field dependence of this correction term over Drüde conductivity. When a magnetic field is applied on a sample affected by weak localization, time reversal symmetry is broken and charge carriers traveling across a loop in one direction or the other will now accumulate a phase term of opposite sign depending on the direction. This term will prevent the two trajectories to interfere constructively toward backscattering, thus suppressing weak localization. As this phase term depends on the magnetic flux through the loop ($\Delta\varphi = 2\pi\frac{\Phi}{\Phi_0}$ where $\Delta\varphi$ is the phase difference between the two paths, $\Phi$ is the flux of magnetic field in the loop and $\Phi_0$ the quantum of flux), bigger loops will lose their coherence more quickly as a function of magnetic field applied than smaller loops. This leads to the experimental signature of weak localization which is a dip in the conductivity of a sample around 0 field applied in magneto-conductance measurements.

### 3.5.2 Weak antilocalization

We just saw how interferences of two time reversed paths induce an enhanced backscattering and a reduction of conductivity. In the presence of spin-orbit interaction though, these interferences will have the opposite effect. Previously we didn't consider the spin of the charge carriers, but spin orbit interaction links a particle spin with its motion. A charge carrier traveling in a sample in presence of spin-orbit interaction will feel an effective magnetic field. In the scope of the D'Yakonov-Perel spin relaxation mechanism, this effective field will induce a rotation of the electron spin as it travels in the sample.

Following the pioneering work of Bergmann [12], we can consider an electron traveling in a diffusive system across a loop. Along this trajectory, the spin $\vec{s}$ will be rotated by a number of random infinitesimal angles (between scattering events in the case of D'Yakonov-Perel spin relaxation mechanism and during scattering events in the case of Elliott-Yafet mechanism). These small rotations will induce a final rotation $R$ such as the end spin state $\vec{s}'$ can be written as $\vec{s}' = R\vec{s}$. An electron traveling the same loop, but in the opposite direction will feel the same internal fields but of opposite direction and in reverse order such as its end state $\vec{s}''$ can be written $\vec{s}'' = R^{-1}\vec{s}$ (see fig.3.4).

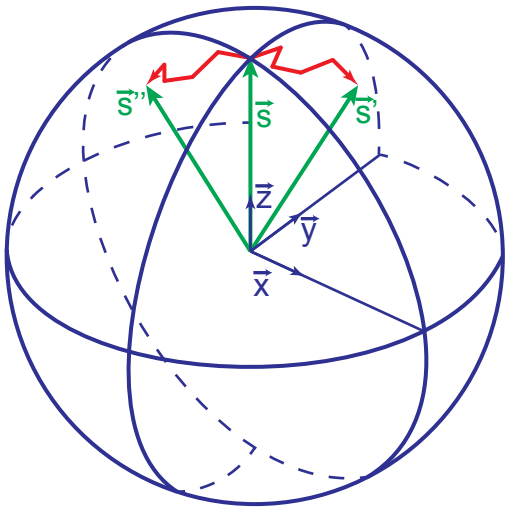


**Fig. 3.4:** Schematic representing the electron spin rotation induced by traveling across a loop in one direction ($\vec{s} \rightarrow \vec{s}'$) compared to traveling the opposite direction ($\vec{s} \rightarrow \vec{s}''$). Taken from [12]

As the interference term between the waves of the two electrons going across the loop in one direction or the other is proportional to $\langle s' \mid s'' \rangle = \langle s \mid R^{\dagger 2} \mid s \rangle$ we will know focus on the $R$ matrix. Using Euler's angles $\alpha$, $\beta$ and $\gamma$ we can write the spin rotation matrix as [13]:

$$R = \begin{bmatrix} \cos\left(\frac{\alpha}{2}\right) e^{i(\beta+\gamma)/2} & i\sin\left(\frac{\alpha}{2}\right) e^{-i(\beta-\gamma)/2} \\ i\sin\left(\frac{\alpha}{2}\right) e^{i(\beta-\gamma)/2} & \cos\left(\frac{\alpha}{2}\right) e^{-i(\beta+\gamma)/2} \end{bmatrix} \tag{3.8}$$

leading to:

$$R^{\dagger 2} = \begin{bmatrix} \cos^2\left(\frac{\alpha}{2}\right) e^{-i(\beta+\gamma)} - \sin^2\left(\frac{\alpha}{2}\right) & -\frac{i}{2}\sin(\alpha)\left(e^{i\gamma} + e^{-i\beta}\right) \\ -\frac{i}{2}\sin(\alpha)\left(e^{i\beta} + e^{-i\gamma}\right) & \cos^2\left(\frac{\alpha}{2}\right) e^{i(\beta+\gamma)} - \sin^2\left(\frac{\alpha}{2}\right) \end{bmatrix} \tag{3.9}$$

Considering a spin $\vec{s}$ such as $\vec{s} = (a, b)$ we now have:

$$\begin{aligned} \langle s' \mid s'' \rangle = \langle s \mid R^{\dagger 2} \mid s \rangle = \cos^2\left(\frac{\alpha}{2}\right)\left[aa^* e^{-i(\beta+\gamma)/2} + bb^* e^{i(\beta+\gamma)/2}\right] - \sin^2\left(\frac{\alpha}{2}\right) \\ - \frac{i}{2}\sin(\alpha)\left[ab^*\left(e^{i\gamma} + e^{i\beta}\right) + ba^*\left(e^{-i\beta} + e^{-i\gamma}\right)\right] \end{aligned} \tag{3.10}$$

As previously mentioned, this term $\langle s' \mid s'' \rangle$ enters in the back scattering probability, but as an average over all possible paths. In the limit of strong spin orbit interaction, the spin loses memory of its initial value quickly, and the end results $\vec{s}'$ and $\vec{s}''$ can take any orientation, but are still linked one to the other. This induces that all angles $\alpha$, $\beta$ and $\gamma$ are random and all terms in $\langle s' \mid s'' \rangle$ average to 0 except for the term $-\sin^2\left(\frac{\alpha}{2}\right)$. This leads to:

$$\langle \langle s' \mid s'' \rangle \rangle = \langle -\sin^2\left(\frac{\alpha}{2}\right) \rangle = -\frac{1}{2} \tag{3.11}$$

This result implies that in a sample with strong spin orbit interaction, the back scattering probability of electrons is reduced by a factor 1/2, leading to an increase of the conductance compared to the standard Drüde conductivity. Similarly to weak localization, weak antilocalization effect is destroyed by an out of plane magnetic field due to time reversal symmetry breaking. This leads to a peak in conductivity around zero field in magneto-conductance measurements.

# References


[1] Shahar Ben-Menahem. The thomas precession and velocity-space curvature. *Journal of Mathematical Physics*, 27(5):1284–1286, 1986.

[2] Christoph Kloeffel, Mircea Trif, and Daniel Loss. Strong spin-orbit interaction and helical hole states in ge/si nanowires. *Phys. Rev. B*, 84:195314, Nov 2011.

[3] Jim Phillips. *Bonds and bands in semiconductors*. Elsevier, 2012.

[4] R Winkler, Dimitrie Culcer, S J Papadakis, B Habib, and M Shayegan. Spin orientation of holes in quantum wells. *Semiconductor Science and Technology*, 23(11):114017, 2008.

[5] Rai Moriya, Kentarou Sawano, Yusuke Hoshi, Satoru Masubuchi, Yasuhiro Shiraki, Andreas Wild, Christian Neumann, Gerhard Abstreiter, Dominique Bougeard, Takaaki Koga, and Tomoki Machida. Cubic rashba spin-orbit interaction of a two-dimensional hole gas in a strained-ge/sige quantum well. *Physical review letters*, 113(8):086601, 2014.

[6] G. Dresselhaus. Spin-orbit coupling effects in zinc blende structures. *Phys. Rev.*, 100:580–586, Oct 1955.

[7] Yu A Bychkov and E I Rashba. Oscillatory effects and the magnetic susceptibility of carriers in inversion layers. *Journal of Physics C: Solid State Physics*, 17(33):6039, 1984.

[8] R J Elliott. Theory of the effect of spin-orbit coupling on magnetic resonance in some semiconductors. *Physical Review*, 96(2):266, 1954.

[9] Y Yafet. Conduction electron spin relaxation in the superconducting state. *Physics Letters A*, 98(5):287–290, 1983.

[10] MI Dyakonov and VI Perel. Spin relaxation of conduction electrons in noncentrosymmetric semiconductors. *Soviet Physics Solid State, Ussr*, 13(12):3023–3026, 1972.

[11] Sudip Chakravarty and Albert Schmid. Weak localization: The quasiclassical theory of electrons in a random potential. *Physics Reports*, 140(4):193 – 236, 1986.

[12] G. Bergmann. Weak anti-localization—an experimental proof for the destructive interference of rotated spin 1/2. *Solid State Communications*, 42(11):815 – 817, 1982.

[13] Richard P Feynman, Robert B Leighton, Matthew Sands, and R Bruce Lindsay. The feynman lectures on physics, vol. 3: Quantum mechanics, 1966.

# Chapter 4

# Germanium/Silicon core/shell nanowires

## 4.1 Introduction

In order to create quantum dots, one has to reduce the dimensionality of the system to 0 [1]. Thus it is a good idea to start with a system that already has reduced dimensionality. One of the standard approaches for this is the use of heterostructures that give rise to two-dimensional electron or hole gas (2DEG and 2DHG, respectively) thanks to the use of a proper stack of materials creating a 2D quantum well. Electrostatic gating is then used to constrain the charges in the last two dimensions. This method has seen extended effective use in systems such as GaAs/AlGaAs heterostructures [2], strained Si [3] or strained Ge as will be detailed later.

The second approach consists in the use of nanowires. A nanowire gets its name from its shape and size as it is usually a cylinder of a few tens of nanometers in diameter and a few microns in length. Electronic transport in nanowires is constrained in two dimensions, leaving only one dimension to be constrained in order to create quantum dots. As of today, in quantum transport, III-V materials have seen the most use, such as InAs [4] or InSb [5] nanowires, but type IV materials such as Ge/Si core shell nanowires are receiving consid-

erable interest, owing to their attractive properties for quantum spintronics applications community due to several advantages.

The qualitative band diagram of core/shell Ge/Si nanowires along the radial direction is shown in the right panel of Fig.4.1. The Ge core forms a quantum well for holes[6]. This type of nanowires presents several advantages, including low hyperfine interaction and strong spin-orbit coupling, as discussed in chapter 1.

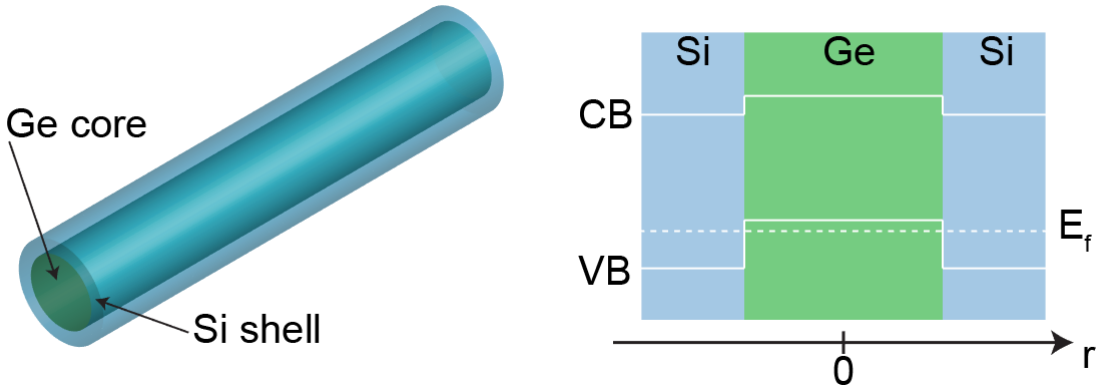


**Fig. 4.1: Left:** Schematic of a Ge/Si core/shell nanowire showing the Ge core in green and the Si shell in blue **Right:** Schematic of the radial band diagram of a Ge/Si core/shell nanowire. The offset of the valence band (VB) and conduction band (CB) creates a quantum well in the Ge core due to the relative position of the Fermi energy ($E_f$)

## 4.2 Device fabrication

### 4.2.1 Substrate preparation

The fabrication of the devices aims at the creation of electrostatic barriers in the nanowires in order to define a double quantum dot. The approach taken is the one of bottom gates in order to reduce to a maximum the number of fabrication steps seen by the wire once it is deposited on the sample. It is usually accepted fabrication steps such as electronic lithography or resist baking have a non negligible chance to induce defects in very fragile structures such as core-shell nanowires. Since the measurement we are aiming at are very sensitive to any defect in the structure, it is best to create a device fabrication

process that involves the strict minimum of steps after the nanowire is deposited, that is to say just contact metal deposition.

With this problematic in mind, the process starts with the fabrication of alignment marks as well as anti-break pads on an undoped $SiO_2$ wafer through electronic beam (e-beam) lithography. The alignment marks will be used in the next lithography steps for realignment of the optical masks for optical lithography steps or of the masker for the electron beam lithographies. The anti-break pads will be used as a link between the contacts and the bonding pads, as will be detailed later. A bilayer of electronic sensitive resist (PMMA/MMA, PMMA 4%) is exposed through electronic beam lithography by a 100 kV JEOL masker and 10/40 nm of Cr/Au is then deposited on the surface by metallic evaporation. The use of a bilayer resist rather than a monolayer one aims at creating an undercut in the resist, thus helping with the lift-off.

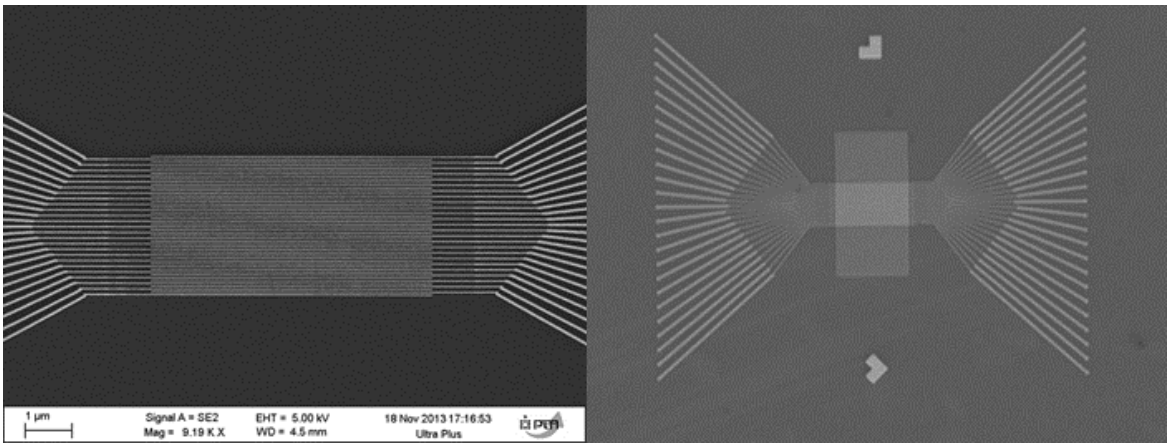


**Fig. 4.2:** **Left:** Scanning electron microscope image of an array of interdigital gates. The gates are made of 5/15 nm of Ti/Au and have a 60 nm pitch **Right:** Scanning electron microscope image of the gate array after deposition of 12 nm of $HfO_2$ dielectric (center of the image)

In between each step, the wafer is thoroughly cleaned by three baths in acetone, ethanol and isopropanol of 5 minutes each in ultrasounds to remove any residues that might affect the rest of the process. The following step is the creation of the bottom gates. A thin layer of PMMA 2% is exposed by e-beam lithography creating an array of interdigital gates. These gates are separated by 60 nm center to center and the linear exposure used in

the masker allows for a fine control of their width of 25 nm. After development, 5/15 nm of Ti/Au is deposited by metallic evaporation (see Fig. 4.2 left).

After this, a dielectric film is deposited on the gates to prevent electrical contact between the gates and the nanowire. To do so, a layer of AZ1512HS optical resist is first deposited on the wafer. In this resist, windows are then opened on top of the gates arrays by optical lithography. Through atomic layer deposition (ALD), 12 nm of the high-$\kappa$ dielectric $HfO_2$ is deposited at 120°C. The excess dielectric is then removed along the resist through lift-off (see Fig. 4.2 right).

The final step before nanowire deposition is the fabrication of bonding pads. The purpose of these pads is to link the microscopic world of our devices to the macroscopic environment of the measurement setup. Once again a layer of AZ1512HS is deposited on the wafer and exposed by optical lithography. Then 10/100 nm of Cr/Au is deposited to create the pads.

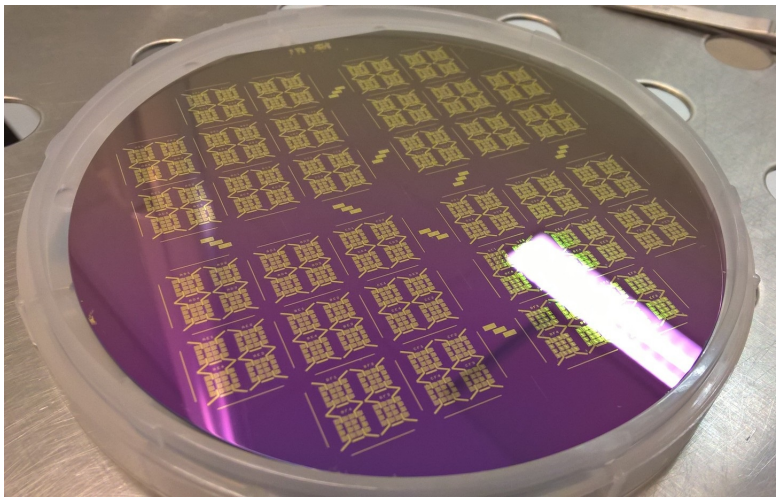

**Fig. 4.3:** Image of a full 4 inches wafer after bonding pads deposition. This wafer contains 128 different chips.

At this step, the wafer is cut in separate chips that will be processed independently. Before nanowire deposition each sample goes through 5 min of oxygen plasma. The main purpose of this step is to remove any resist residue on the surface but it has also been shown that a step of oxygen plasma on a $SiO_2$ substrate prior to the deposition of InSb nanowires can improve their low temperature conductivity [7].

### 4.2.2 Nanowire deposition

The nanowires used in this work were grown in the group of Charles M. Lieber in Harvard University. They consist of a Ge core of around 15 nm of diameter circled by a shell of around 3 nm of thickness. The fabrication process has been detailed elsewhere [8].

Nanowires can be deposited on the gates using a nanomanipulator consisting of a tungsten tip with a 350 nm end radius fixed on a commercial 3-axis stage (see Fig. 4.4). Under an optical microscope, and with the use of the stage, the tip is lightly brushed over the nanowire substrate until a wire can be seen on the tip. The tip is then moved on top of a field of the processed chip and the nanowire is gently deposited across the gates (see Fig. 4.5 left).

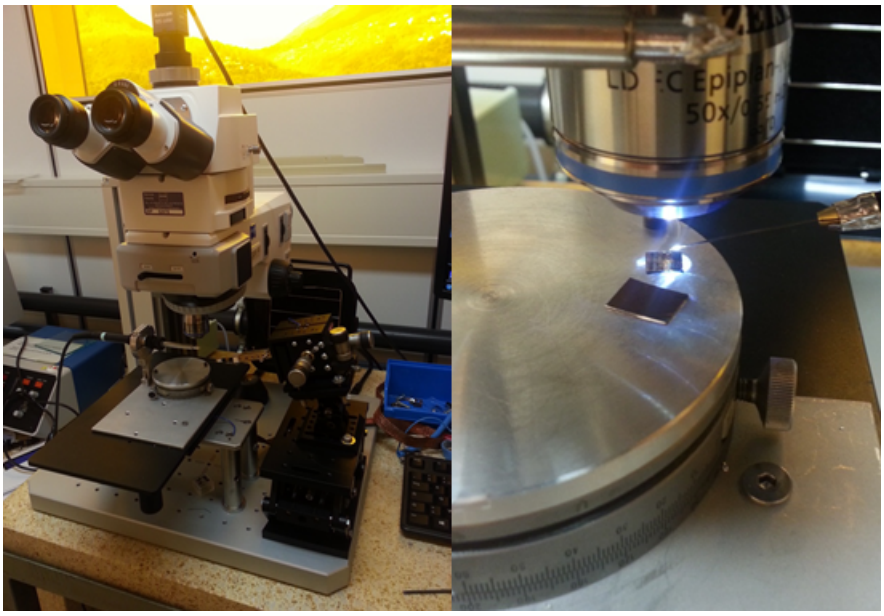

**Fig. 4.4:** **Left:** Picture of the microscope and the nanomanipulator **Right:** Closer image of the tungstene tip with the sample and the nanowire substrate

The chip is then imaged under a scanning electronic microscope (SEM) in order to identify which of the gates fields have a single nanowire properly lying on top of the gates. The imaging is done quickly and at low acceleration voltage (1 kV) in order to minimize the possible damages to the nanowires and the deposition of charges and carbon atoms on the surface that the electron beam could induce.

Due to their long length relative to their diameter, the nanowires do not stay straight on the surface but tend to bend and tangle, forming bundles and making it hard to pick individual wires. Still, the technique is reliable enough that out of the 64 fields per chip onto which wires are deposited, around 10 usually present a single nanowire laying correctly across the gate. This provides a sufficient yield given that only 7 wires can be fully contacted due to the required number of pads needed (nine, two for the contacts, three for the barrier gates, two for the plunger gates and two for the contacts gate groups) compared to the number of pads available (64 in our design)

### 4.2.3 Contact fabrication

The sample is then covered with PMMA 4% electronic resist in which the contacts to the wire are written by e-beam lithography. The wire is then dipped for 3 seconds in buffered hydrofluoric acid in order to remove the oxidized shell so that the metal contacts directly the Ge core. By metallic evaporation, 100 nm of Ni is then deposited on the sample (see Fig. 4.5 right). This metal had been chosen as it was the one giving the best combination of both contact yield and resistance among the one accessible by metallic evaporation in the clean room.

The two contacts of the wire are separated by a distance of around 780 nm or 13 times the distance between gates in order to leave exactly 13 gates under the wire in between the contacts. Of these 13 gates, the 5 center ones were contacted individually to independent bonding pads and, during the measurements, were employed as three barrier gates and two plunger gates. The four gates on each sides were shorted in such a way as to form two sets of larger "contact gates", which were then used to act on the contact resistance of the wire.

During the deposition of the contact metal, it is possible that the metal line breaks at the edge of the bonding pads. A possible reason for this phenomenon is that the Au of the bonding pads expands significantly during the contact lines evaporation due to the heat brought by the Ni target. As the sample cools down after the evaporation, the Au retracts, thus applying significant stress on the Ni line that breaks on the step it has to do to go up

the bonding pad. This is why anti-break are processed earlier. At this last step they will be situated both under the bonding pads and the contact lines providing an electrical link between the two even if the Ni line breaks. The much lower thickness of the anti-break (50 nm) compared to the bonding pads (110 nm) makes significantly more reliable the contact of the Ni line (100 nm thick) with the anti-break rather than with the bonding pads.

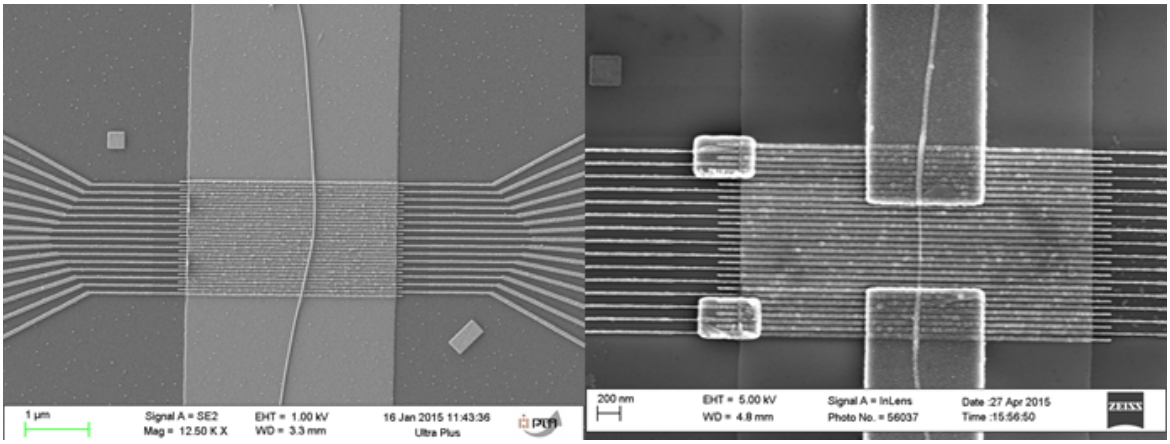


**Fig. 4.5: Left:** Scanning electron microscope image of a nanowire deposited across the gates. These Ge/Si nanowires are approximately 20 nm of diameter and a few microns in length **Right:** Scanning electron microscope image of a finished device showing a wire contacted by two metal leads

The sample is then ready to be measured.

## 4.3 Measurements

### 4.3.1 Experimental setup

In order to observe quantum effects in electronic transport, one has to perform measurements at low temperature. Indeed, the energy scales of the phenomena to be observed are so small that the measurement temperature has to be low enough so that the temperature energy scale $k_bT$ (where $k_b$ is the Boltzmann constant and T is the temperature) is significantly smaller than the ones of the phenomena. It is for this reason that all the

measurements detailed in this section were performed in a $^3$He fridge capable of reaching a base temperature of around 250 mK.

The chip to be measured is glued on a sample holder that will serve as an interface between the device and the measurement setup. The silver paste used to glue the sample is a material with both high thermal and electrical conductivity in order to ensure a good thermalization of the sample with the fridge and a uniform ground level as reference for all electric potentials in the sample. The bonding pads of the device are each connected one of the 24 line of the sample holder by 25 µm diameter aluminum wire wedge bonded through a commercial bonding machine. The sample holder is then plugged on the cold finger of the $^3$He fridge.

Similarly to the sample holder, the fridge is equipped with 24 DC lines connecting the cold finger to the outside world. Each of these line possesses an RC filter with a cutoff frequency of 100 kHz to minimize high frequency excitation from the environment to go in the sample and to help thermalizing the electrons. My previous work in this exact fridge have shown good agreement between the fridge measured temperature and the electronic temperature [9].

The battery powered low-noise electronic used for transport measurements was developped by Raymond Schouten at the QT laboratory in Delft

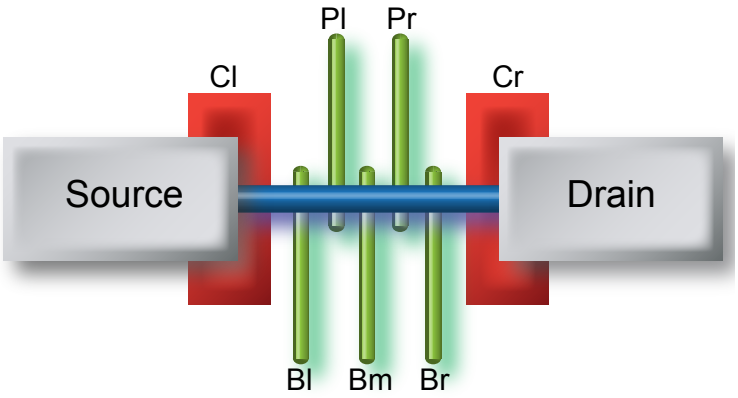


**Fig. 4.6:** Schematic of the measured device. The nanowire (blue) lies on top of 5 individual gates (green) and two sets of shorted gates (red) going under the Ni contacts (grey)

### 4.3.2 Gate capacitance

Once the sample is cooled down to base temperature, a bias is applied across the nanowire and the current going through it is measured. Sweeping the bias from -10 mV to +10 mV while keeping all the gates grounded, no current goes through the wire at small bias (from -0.8 to +1.2 mV approximately) (see Fig. 4.7). This can be explained by a Coulomb blockade effect in the wire due to the presence of tunnel barriers at the interfaces between the nanowire and the contacts. The nanowire is not conducting without a large enough bias. Applying negative voltage on the sets of gates under the contacts reduces the strength of the contact barriers thus increasing the conductance of the system but does not entirely remove the Coulomb blockade effect.

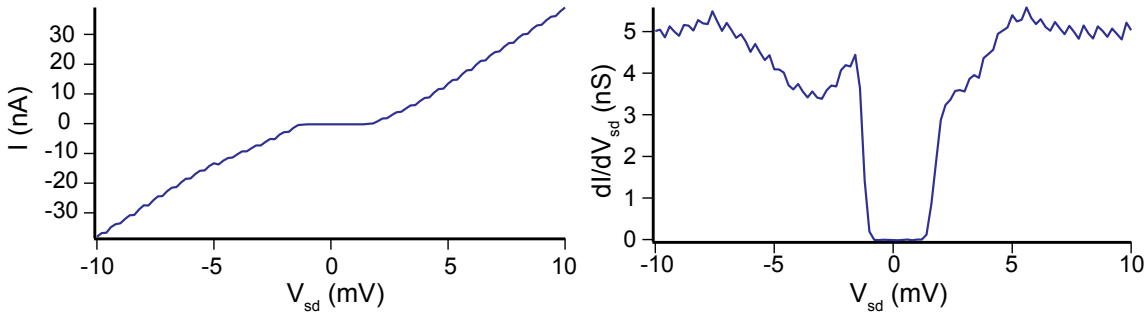


**Fig. 4.7: Left:** Current (I) as a function of source drain voltage ($V_{sd}$) in the full wire with no voltage applied to any gate **Right:** Differential conductance ($dI/dV_{sd}$) as a function of source drain voltage ($V_{sd}$) in the full wire with no voltage applied to any gate

Applying no DC bias across the wire and applying AC voltage with the help of a lock-in, allows for the readout of the differential conductance of the system. By sweeping one of the bottom gates we observe a series of conductance peaks (see Fig. 4.8). This effect is referred to as Coulomb peaks and confirms the presence of a quantum dot in the wire due to the barriers at the contacts (see chapter 2.1.3). In figure 4.8 we can observe 55 regularly spaced peaks on a span of 2 V of a bottom gate, the left plunger in this specific case. Similar results are observed for all individual gates. The invariance of the spacing between the peaks over a large number of transitions tends to indicate that the dot is in a regime where the number of holes it includes is large enough so that the Coulomb

charging energy $e^2/C_T$ where $e$ is the quantum of charge and $C_T$ is the total capacitance of the dot to its environment, is the dominant component in the addition energy, and the dot is behaving mostly as a single-electron metallic transistor, with negligible mean level spacing (see chapter 2.1.2).

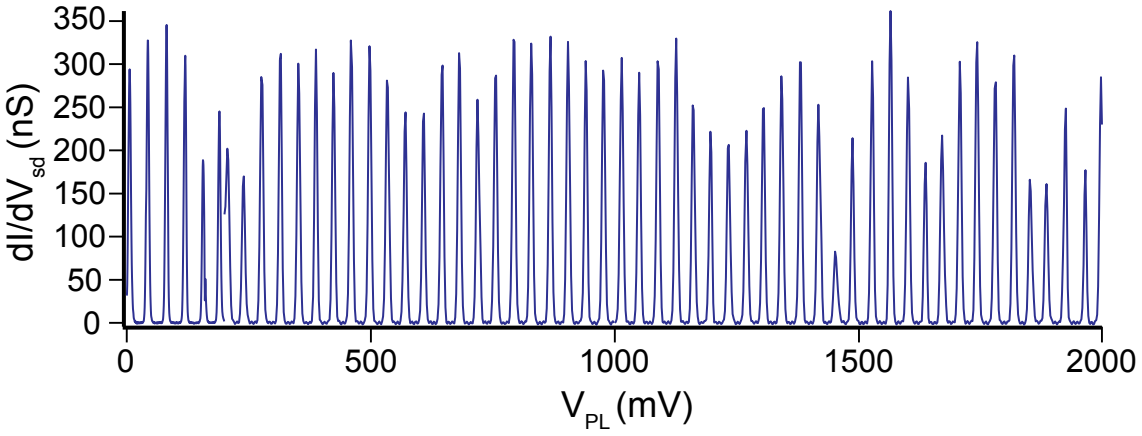


**Fig. 4.8:** Differential conductance $dI/dV_{sd}$ as a function of PL gate voltage $V_{PL}$ showing 55 regularly spaced Coulomb peaks over a span of 2 V of gate voltage

Measuring the bias dependence of these peaks results in the characteristic Coulomb diamonds (see Fig. 4.9). From the size of diamonds along the bias voltage axis, we can extract the charging energy of the dot (see chapter 2.1.4). We find a charging energy of around 1.2 meV. The reproducible shape and size of this series of diamonds confirm the large number of charges and the metallic character of the dot. From the value of the charging energy we deduce a total capacitance of the system $C_T$ = 133 aF, which corresponds to the sum of the capacitances between the dot and all the elements in its environment (mostly the gates and the source and drain electrodes). Knowing that the gate-voltage spacing $\Delta V_g$ between two consecutive Coulomb peaks is 36 mV, we can deduce the capacitance of an individual gate $C_g$ from the formula $C_g = e/\Delta V_g$. All individual gates have the same value of around $C_g = 4$ aF. This value is consistent with the value $C_{th} = 9$ aF expected for a 20 nm × 20 nm overlap of the nanowire on the gate, the two being separated by 12 nm of hafnium oxide.

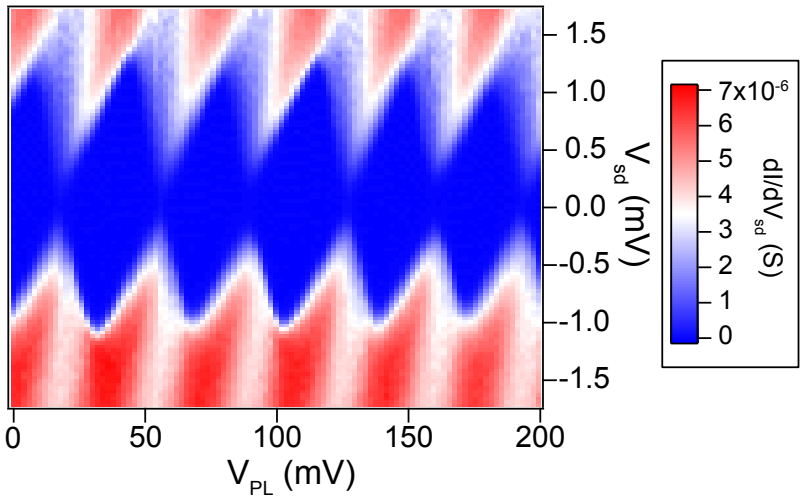


**Fig. 4.9:** Differential conductance $dI/dV_{sd}$ in the wire as a function of PL gate voltage $V_{PL}$ and bias $V_{sd}$ with no voltage applied on the other gates. The regular shape and size of the Coulomb diamonds indicate a dot with a large number of charges

By sweeping the gates under the contacts, it is possible to increase the conductivity in the wire. Doing so reveals the same type of conductance peaks but with a different periodicity. Sweeping the barrier under the right contact (CR) (see Fig. 4.10 left) we observe that the periodicity changed to 9 mV. This is easily explained by the fact that the CR activates 4 individual gates under the wire, thus increasing the capacitance to the dot by a factor 4. On the other hand, sweeping the gate under the left contact only reduces the periodicity by a factor 2.6 (see Fig. 4.10 right). This is most likely due to an overlap of the Ni contact on one of the gates or due to a broken gate.

### 4.3.3 Double dot system

By properly adjusting the voltages applied to the local gates, it is then possible to split the quantum dot in two. The middle gate (BM) is swept to +4 V in order to create a barrier in the middle of the wire, thus splitting the dot. The gates under the contacts CR and CL are then used as plungers for the two dots. Plotting the differential conductance of the wire as a function of the voltage applied on the contact gates shows that conduction in the wire only happens in small, regularly spaced regions (see Fig. 4.11). This is to be

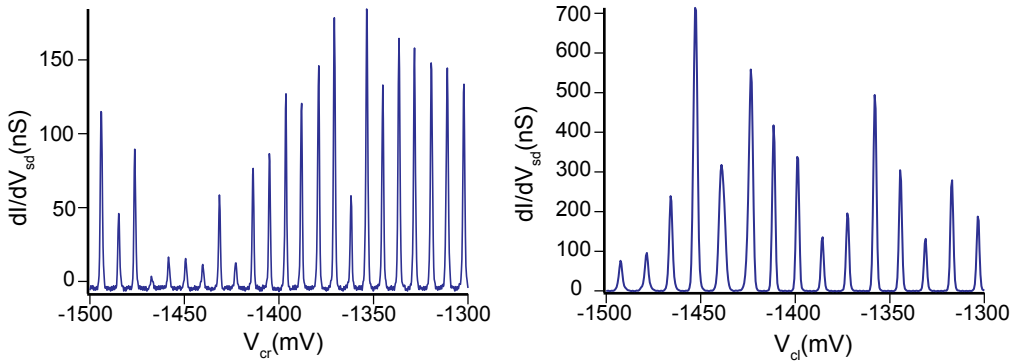


**Fig. 4.10:** Differential conductance $dI/dV_{sd}$ measurement of the wire as a function of right (left graph) and left contact gates (right graph). The periodicity of the Coulomb peaks is different from sweeps of an individual gate

expected from a double dot system where the system can only conduct when both dots are conducting (see chapter 2.2.1). It has to be noted that the spacing between conducting resonances for a given gate is the same as the one previously observed with only one dot. This shows that the contact gates have really low effect on the opposite side of the wire even when it is not split in two. The fact that the resonances are aligned on almost completely vertical or horizontal lines further confirm that there is no cross capacitance of one gate to the opposite dot.

In order to observe quantum effects such as Pauli spin blockade in a double dot system, one has to reduce the number of charges in the dots. To do so, the external barrier gates BL and BR are progressively swept to observe the transition from a plunger effect to a barrier effect (see Fig. 4.12). When applying low voltages on the gates, they will act as plungers for the two metallic dots observed before (see Fig. 4.12 a). As the voltage on the gates is increased, they will start creating a barrier. The resulting potential can be quite complicated as the charges will not yet be completely localized between barriers (see Fig. 4.12 b). Only when the voltage applied on the gates is high enough will the barriers allow for the system to be considered as a double dot and the characteristic double triangle resonances can be observed (see Fig. 4.12 c). We notice that some of the transitions expected are missing or have a much lower current than the others. This is most likely due to the presence of other dots in series between the barriers and the contacts.

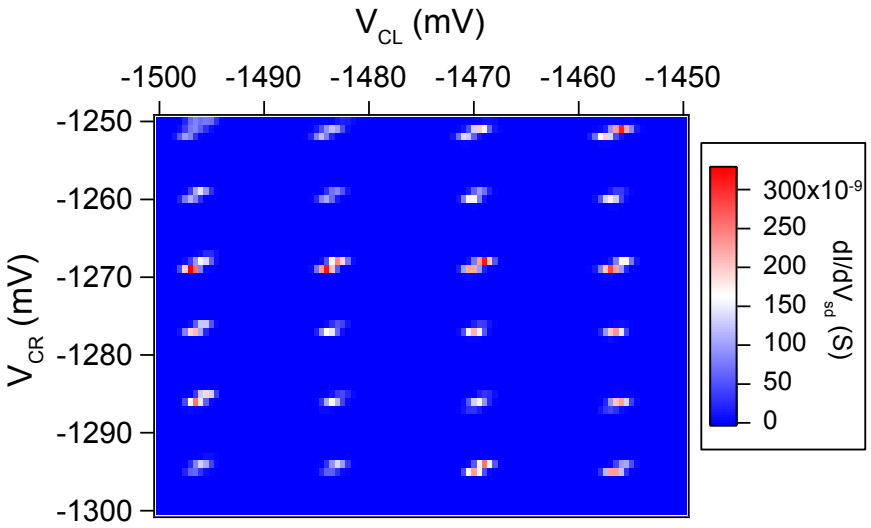


**Fig. 4.11:** Differential conductance $dI/dV_{sd}$ of the wire as a function of both the left and right contact gate voltages $V_{CL}$ and $V_{CR}$ respectively, with a barrier created in the middle of the wire by BM ($V_{BM}$= 4 V)

In order to get rid of the effects of the parasitic dots, the bias across the wire is increased from 0.5 to 4 mV. This higher bias should keep the parasitic dots in a conducting regime for most of the transitions. For a better confinement, the three barriers BL, BM and BR are raised to +5 V and the two plungers PL and PR are swept. The stability diagram shows the characteristic double triangle resonances of a double dot(see Fig. 4.13). This time the spacing is not regular between transitions, showing the variation of the orbital spacing component of the addition energy. This component becomes of the same order of magnitude as the Coulomb repulsion component only when the number of charges in the dots is small. It is to be noted that the last transitions seen in Fig. 4.13 does not correspond to the last holes in the system as other transition can be observed for higher plunger voltages but with much lower conductance.

When focusing on the barely visible transition highlighted in Fig. 4.13, we can clearly observe a pair of triangles. When observed at a positive bias with no magnetic field applied, the triangles contain three parallel lines corresponding to the ground state and excited-state transitions. In Fig. 4.14, yellow lines highlight the triangles and the base line as they can be seen with no magnetic field and a +4 mV bias. The same lines (reversed

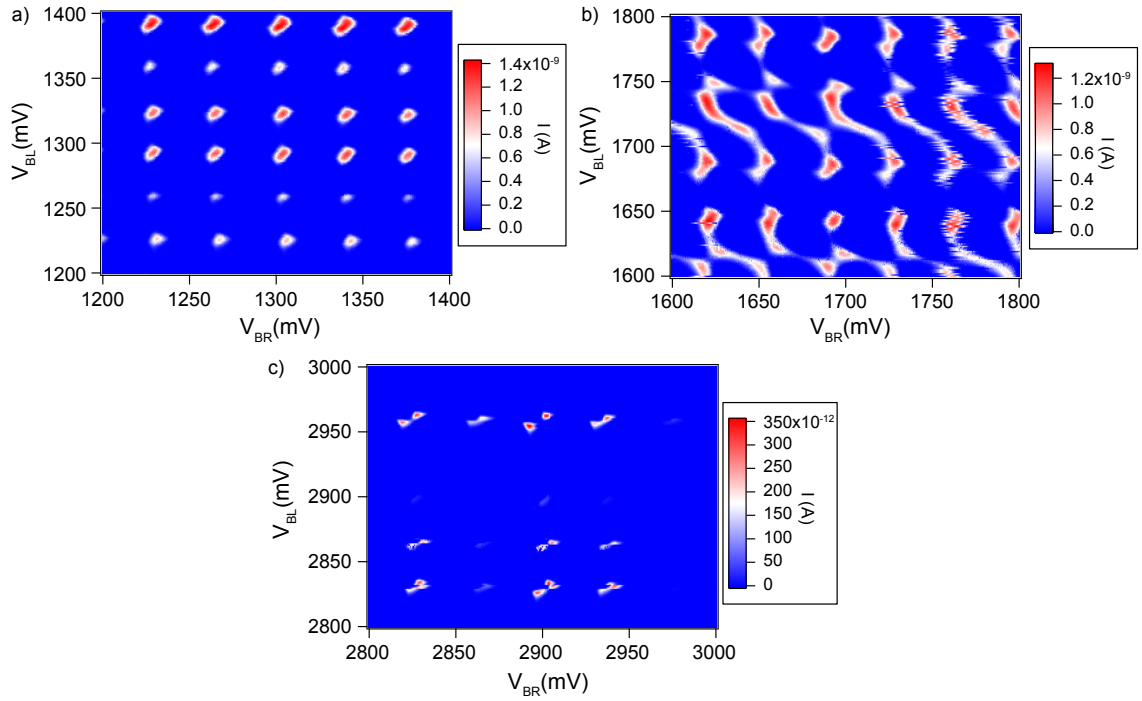


**Fig. 4.12:** Stability diagram of the double dot system as a function of gates BL and BR. At lower gate voltage (a), the dots are confined between the middle barrier (BM) and the contacts. As the gate voltages are increased, the gates BR and BL start creating barriers (b) and the dots end up confined between the the middle barrier BM and the two side barriers BL and BR (c)

for negative bias) have been reproduced in the other situations in order to highlight the differences. When reversing the bias, the direction of the triangles changes as expected (see Fig. 4.14b). The size of the triangles is also reduced, which can be explained by the asymmetry of the bias applied across the double dot system. Going back to positive bias but applying magnetic field perpendicular to the nanowire and the sample, the base line of the triangles fades away at +2 T (Fig. 4.14c) and completely disappears at +4 T (fig. 4.14d). This behavior is a characteristic signature of Pauli spin blockade where the hole in the left dot cannot tunnel to the right dot because its forms a triplet state with the spin of the hole in the right dot. The system is then blocked and current is suppressed (see chapter 2.2.3).

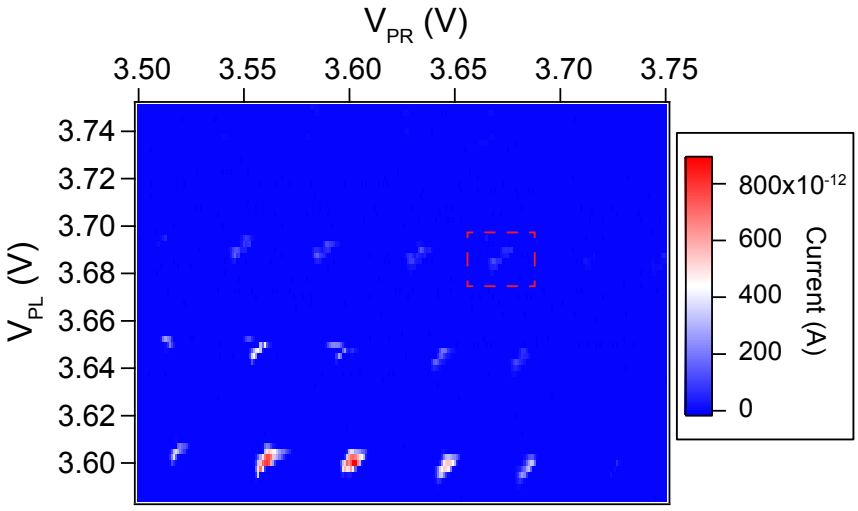


**Fig. 4.13:** Stability diagram of the studied double dot system, with the dots on top of PL and PR. The red dashed box highlights the studied transition.

## 4.4 Conclusion

After measuring the data shown in this chapter, the device ceased to function, due to an accidentally large voltage spike and unfortunately we were not able to reproduce a fully working and stable device after this one.

At the moment of this experiment, two major factors were affecting the number of devices that could be effectively measured a low temperature. The first one was the yield on the fabrication of the finger gates. Due to the technicality of the gate fabrication process, most of the devices would have at least one broken gate. This would be synonym to a floating potential below the wire which would induce high instability of the device. The fabrication process was improved shortly after these experiment and fully working substrates could be produced more reliably.

The second limiting factor on the number of device measured was the contact resistance. The majority of the devices exhibited a room temperature resistance above 200 kΩ. Such high resistance would result in an insulating behavior at low temperature. To remedy this issue, it was then decided to add to the fabrication process a step of annealing of the contacts in Ar gas at 300°C for 10 minutes, after contacts deposition. This added

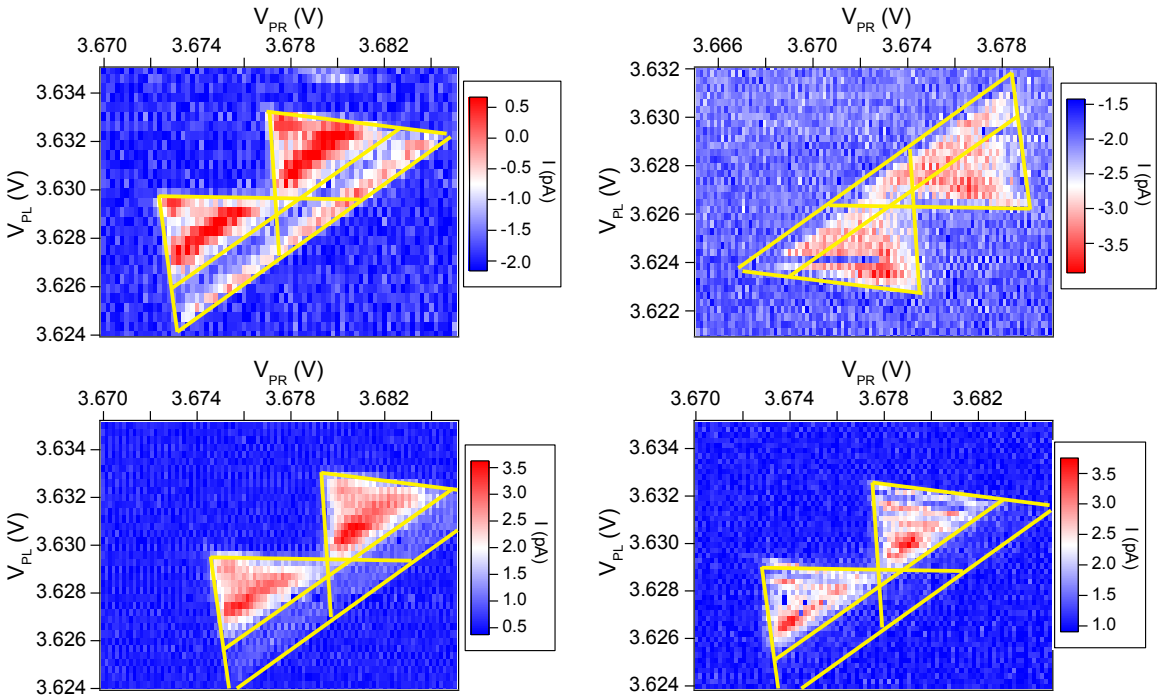


**Fig. 4.14:** The same double triangle at different bias and magnetic field. **a):** $V_{SD}$=4 mV and no magnetic field. **b):** $V_{SD}$=-4 mV and no magnetic field. **c):** $V_{SD}$=4 mV and B = 2 T. **d):** $V_{SD}$=4 mV and B= 4 T

step allowed for a more reliable production of devices with room temperature resistance of around 100 kOhm that were conducting at low temperature.

Unfortunately, while both these issues were fixed shortly after measuring the sample presented earlier, a lot more devices were measured but none of them was stable enough to reproduce these results and go further. I now believe that this instability was due to the annealing step. I later became aware of a work on rapid thermal annealing of pure germanium nanowires with nickel contacts [10] showing a 56.3% lattice mismatch between the $Ni_2Ge$ germanide phase formed by annealing and the Ge of the wire. This mismatch can induce the formation of nanoclusters of $Ni_2Ge$ on the surface of the nanowire. While none of these clusters have been observed on our wires after annealing, it is likely that this mismatch will create additional strain on the very fragile Si shell. Defects in the shell can explain the instability of the wires measured.

# References


[1] Leo P Kouwenhoven, Charles M Marcus, Paul L McEuen, Seigo Tarucha, Robert M Westervelt, and Ned S Wingreen. Electron transport in quantum dots. In *Mesoscopic electron transport*, pages 105–214. Springer, 1997.

[2] M. Ciorga, A. S. Sachrajda, P. Hawrylak, C. Gould, P. Zawadzki, S. Jullian, Y. Feng, and Z. Wasilewski. Addition spectrum of a lateral dot from coulomb and spin-blockade spectroscopy. *Phys. Rev. B*, 61:R16315–R16318, Jun 2000.

[3] L. J. Klein, K. A. Slinker, J. L. Truitt, S. Goswami, K. L. M. Lewis, S. N. Coppersmith, D. W. van der Weide, Mark Friesen, R. H. Blick, D. E. Savage, M. G. Lagally, Charlie Tahan, Robert Joynt, M. A. Eriksson, J. O. Chu, J. A. Ott, and P. M. Mooney. Coulomb blockade in a silicon/silicon-germanium two-dimensional electron gas quantum dot. *Applied Physics Letters*, 84(20):4047–4049, 2004.

[4] S Nadj-Perge, SM Frolov, EPAM Bakkers, and Leo P Kouwenhoven. Spin-orbit qubit in a semiconductor nanowire. *Nature*, 468(7327):1084–1087, 2010.

[5] VS Pribiag, S Nadj-Perge, SM Frolov, JWG van den Berg, I van Weperen, SR Plissard, EPAM Bakkers, and LP Kouwenhoven. Electrical control of single hole spins in nanowire quantum dots. *Nature nanotechnology*, 8(3):170–174, 2013.

[6] Jie Xiang, Wei Lu, Yongjie Hu, Yue Wu, Hao Yan, and Charles M Lieber. Ge/si nanowire heterostructures as high-performance field-effect transistors. *Nature*, 441(7092):489–493, 2006.

[7] I Van Weperen. *Quantum Transport in Indium Antimonide Nanowires: Investigating building blocks for Majorana devices*. PhD thesis, 2014.

[8] Wei Lu, Jie Xiang, Brian P Timko, Yue Wu, and Charles M Lieber. One-dimensional hole gas in germanium/silicon nanowire heterostructures. *Proceedings of the National Academy of Sciences of the United States of America*, 102(29):10046–10051, 2005.

[9] P. Torresani, M. J. Martínez-Pérez, S. Gasparinetti, J. Renard, G. Biasiol, L. Sorba, F. Giazotto, and S. De Franceschi. Nongalvanic primary thermometry of a two-dimensional electron gas. *Phys. Rev. B*, 88:245304, 2013.

[10] Jianshi Tang, Chiu-Yen Wang, Faxian Xiu, Yi Zhou, Lih-Juann Chen, and Kang L Wang. Formation and device application of ge nanowire heterostructures via rapid thermal annealing. *Advances in Materials Science and Engineering*, 2011, 2011.

# Chapter 5

# Weak antilocalization in strained germanium heterostructure

While using nanowires and a bottom-up fabrication process can be a versatile enough approach for research challenges, fabricating a quantum computer would require a high number of qubits for which a top-down fabrication process, closer to the standards of the microelectronic industry, would be more reliable. For this reason, using two-dimensional quantum wells in germanium heterostructures can be advantageous as spintronics elements such as quantum dots or quantum point contacts can be easily engineered with a combination of mesa etching and metal gate electrostatic confinement.

In this chapter we use such an heterostructure and a Hall bar device to study the spin orbit interaction in these germanium systems.

## 5.1 Heterostructure description and device fabrication

### 5.1.1 Heterostructure

The heterostructure employed here and illustrated in Fig. 5.1 was grown by the team of Maksym Myronov at Warwick University. On a 200 mm Si (001) wafer, a reverse linearly graded, fully relaxed, virtual substrate of 3 $\mu$m $Si_{0.2}Ge_{0.8}$/Ge/Si(001) was deposited by

RP-CVD (Reduced-Pressure Chemical Vapor Deposition). Using the same technique, with a germane ($GeH_4$) gas precursor, a 32 nm thick Ge epilayer was grown on top, at a temperature lower than 450°C. This low temperature is of the utmost importance for the stability of compressively strained Ge. More details on the heterostructure fabrication can be found in Ref. [1].

The lattice mismatch between $Si_{0.2}Ge_{0.8}$ (a= 5.60 Å) and Ge (a= 5.66 Å) [2] will induce a compressive strain in the Ge epilayer. The germanium epilayer eventually acts as a confining quantum well for a two-dimensional hole gas (2DHG).

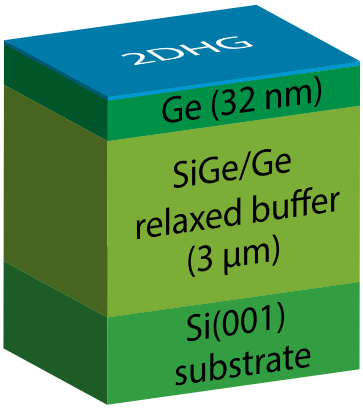


**Fig. 5.1:** Schematic of the heterostructure used in this chapter. On a silicon wafer is deposited a buffer layer of SiGe. On top of this buffer layer, 32 nm of Ge are strained, thus inducing the formation of a 2DHG at the top surface

The presence of the 2DHG at the top surface of the heterostructure confers an advantage in terms of ease of fabrication as no etching is required to contact the hole gas. Moreover, it allows for an efficient control of the confined holes by means of top gate electrodes, due to maximal capacitive coupling.

### 5.1.2 Device fabrication

Device fabrication aims at realizing a Hall bar on this heterostructure in order to perform magneto-transport measurements. Preliminary tests revealed that this undoped

heterostructure is frozen at low temperature. As a result, it becomes necessary to provide the Hall bar with a top gate aimed at inducing the accumulation of the 2DHG.

The first fabrication step consists in the deposition of alignment marks that will be used for realignment of the optical masks used in the next lithography steps. A layer of positive optical resist AZ1512HS is first deposited on the sample. Optical lithography is then performed, thus opening windows in the resist after development. By metallic evaporation, 10/50 nm of Ti/Au is then deposited. After lift off in acetone, the resist and the metal on top is removed leaving only the alignment marks.

We then proceed to mesa etching. The mesa is necessary to prevent the 2DHG to propagate under the accumulation gate pad when a voltage is applied (the structure being frozen at low temperature, only the part below the accumulation gate can be conducting). A second lithography step consisting of negative resist AZ2070HS spinning, exposure and development is performed. This time the lithography will remove all the resist but the one covering the future mesas. We then etch the heterostructure through a $Cl_2/N_2/O_2$ plasma for a depth of 55 nm. The resist on top of the mesa is finally removed with an acetone bath (Fig. 5.2 a).

Ohmic contacts then need to be defined to access the 2DHG. An optical lithography similar to the one used for the alignment marks is used, this time opening windows at the edge of the mesa and further away. A layer of 60 nm of Pt is then evaporated on the sample and we proceed to lift off (Fig. 5.2 b).

As the gas needs to be isolated from the top gate, an oxide has to be deposited. We proceed to the deposition of 30 nm of $Al_2O_3$ by atomic layer deposition (ALD) at temperature of 250 °C.

Finally, a last step of electronic lithography, similar to to the previous ones is performed to create the top gate (the resist used here is PMMA). This lithography opens a window in the resist in a standard 6 terminals Hall bar shape that extends to the edge of the ohmic contacts. The metal of choice here is 10/50 nm of Ti/Au deposited by metallic evaporation. A final lift-off is then performed to remove the resist and the exceeding metal (Fig. 5.2 c and d). The sample is then ready.

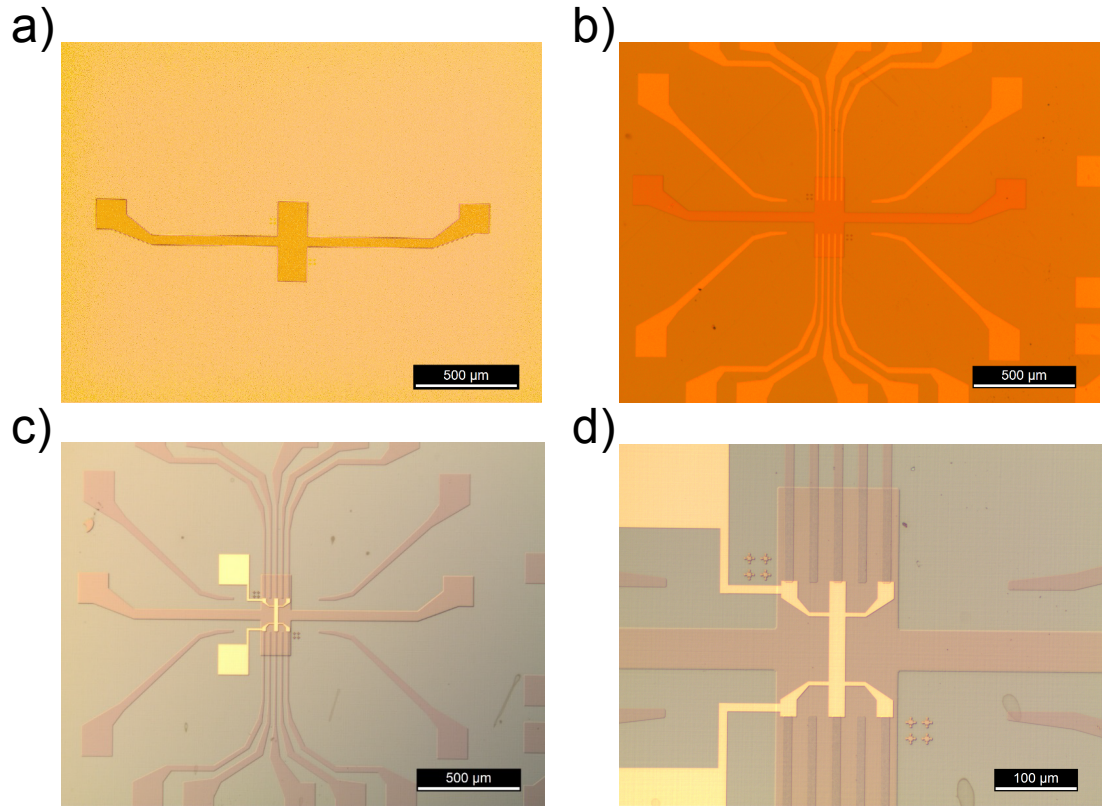


**Fig. 5.2: a):** Optical image of the surface of the heterostructure after etching of the 55 nm deep mesa.**b):** Optical image of the sample after deposition of the 60 nm Pt contacts.**c):** An oxide layer of 30 nm of $Al_2O_3$ is deposited by ALD over the sample and a Ti/Au hall bar shaped accumulation top gate is evaporated on top.**d):** Zoom on the Hall bar shaped top gate

## 5.2 Transport measurements

### 5.2.1 Experimental setup

Similarly to chapter 4, measurements are performed in a $^3$He fridge with a base temperature of around 250 mK. Two of the 24 lines are used to apply a constant current $I_{ch}$ on the channel of the Hall bar. Rather than using a current source for this, we preferred a voltage source used with a serial resistance of 1MΩ in order to protect the sample (when the sample is highly resistive, a current source would try to apply high voltage on the sample and might damage it). A currentmeter is used to control the current going through

the channel. Two pairs of lines are then used to measure the voltage drop across the channel $V_{ch}$ and the Hall voltage $V_H$. Finally, a seventh line is used to apply voltage on the accumulation gate situated on top of the Hall bar.

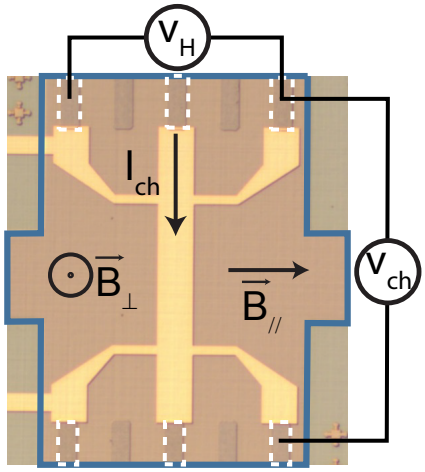


**Fig. 5.3:** Optical image of the Hall bar device. The blue line outlines the mesa and the white dashed lines the Pt contacts. We measure the Hall voltage ($V_H$) and the channel voltage ($V_{ch}$) from which we extract Hall resistivity and channel resistivity respectively. Direction of the two components for the applied magnetic fields is also indicated.

The fridge used is also equipped with a single axis 9 Tesla magnet. In section 5.2.2, the sample is situated in way so that the magnetic field applied is perpendicular to the surface of the Hall bar ($B_\perp$). For the measurements described in section 5.2.3, a mechanical rotator was added in the fridge to allow for the rotation of the sample inside the coil. This leads to the ability to switch from a fully perpendicular field $B_\perp$ to a magnetic field parallel to the 2DHG plane and perpendicular to the conduction channel $B_{//}$ (see Fig.5.3).

### 5.2.2 Gate dependence

As previously mentioned, the hole gas is frozen at low temperature. In order for the system to be conductive, a negative voltage has to be applied on the accumulation gate. In our experiment, the conduction threshold is situated at -3.8 V. Due to leakage through

the oxide starting at higher gate voltage, all the measurements have been performed for a range of gate voltages between -4.1 and -4.4 V.

For each gate voltage value, both the channel voltage $V_{ch}$ and the Hall voltage $V_H$ are measured as a function of out-of-plane magnetic field $B_\perp$. Channel or Hall resistivity is then defined as $\rho_{XX} = V_{ch}/(I_{ch}.N_{sq})$ and $\rho_{XY} = V_H/I_{ch}$ respectively, where $I_{ch}$ is the measured channel current and $N_{sq}$ represents the size of the channel in number of squares $N_{sq} = L/w$ where $L$ and $w$ are the channel length and width respectively. $N_{sq} = 4$ in this sample.

Examples of traces of channel and Hall resistivity as a function of magnetic field are presented in fig.5.4. In red, the channel resistivity most distinctive feature is a dip at zero field. This is a clear sign of weak antilocalization, as will be detailed later.

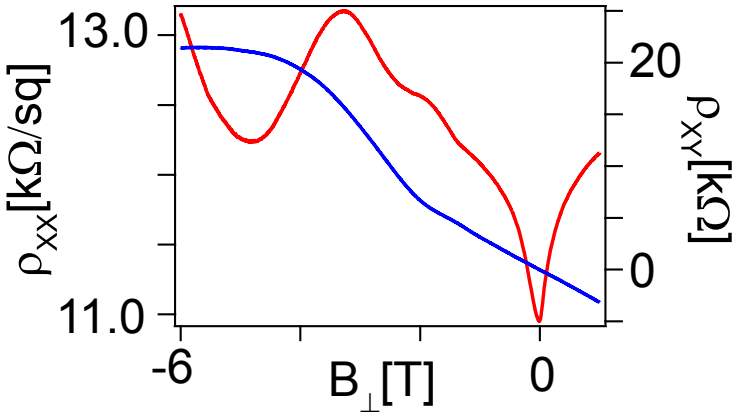


**Fig. 5.4:** Channel resistivity $\rho_{XX}$ (red) and Hall resistivity $\rho_{XY}$ (blue) as a function of out of plane magnetic field $B_\perp$. Channel resistivity shows a dip at low field which is a signature of weak antilocalization.

Traces of Hall resistivity, on the other hand, show a linear dependance with magnetic field for smaller field ($|B_\perp| \leq 2$ T). From this, we can extract the carrier density $n_{hole}$ from the formula:

$$n_{hole} = \frac{B_\perp}{e \times \rho_{XY}(B_\perp)} \tag{5.1}$$

We can then extract the carrier mobility $\mu$ from the channel resistivity at 0 field by:

$$\mu = \frac{1}{e \times n_{hole} \times \rho_{XX}(B_\perp = 0)} \tag{5.2}$$

On the accumulation gate voltage range used during the measurement, that is to say from -4.1 to -4.4 V, we obtained mobility and carrier density ranging from 800 to 2400 $cm^2/Vs$ and 1.3 to 1.7 $\times 10^{11}$ $cm^{-2}$ respectively (see fig. 5.5).

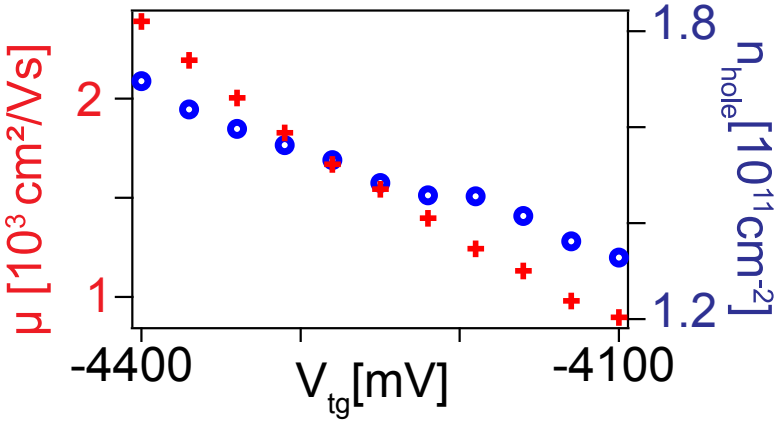


**Fig. 5.5:** Mobility $\mu$ (red) and carrier density $n_{hole}$ (blue) as a function of accumulation gate voltage

When comparing to similar heterostructures [3], our values obtained for mobility are quite low. Additionally, from the evolution of carrier density with gate voltage, it is possible to estimate the capacitance of the accumulation gate. From the Hall measurement we extract a gate capacitance of only 21 $nF/cm^2$, one order of magnitude lower than the expected value of 0.27 $\mu F/cm^2$ for a capacitor with a dielectric made of 30 nm of $Al_2O_3$. We were also able to measure our gate capacitance at room temperature using a gate reflectometry technique [4] and obtained a value of 0.33 $\mu F/cm^2$, in good agreement with the expected value. We explain both the low mobility and gate capacitance by a high number of traps at the interface between the germanium epilayer and the oxide layer as will be explained later.

As previously mentioned, the traces of channel resistivity as a function of magnetic field show a dip at 0 field, a sign of weak antilocalization (WAL) which is a positive correction to conductivity over the Drüde model. In order to understand the magnetic field

dependance of our system, we can consider the channel conductivity as being a sum of three contributions: the Drüde conductivity $\sigma_D$, the WAL correction to conductivity $\Delta\sigma_{WAL}$, and a third term $\sigma_{offset}$ regrouping all contributions that are not magnetic field dependent, such as hole-hole interaction.

$$\sigma_{XX} = \sigma_D + \Delta\sigma_{WAL} + \sigma_{offset} \tag{5.3}$$

To extract the WAL contribution to conductivity, we first need to subtract the Drüde conductivity term which dependance on magnetic field is given by:

$$\sigma_D(B) = \frac{en_{hole}\mu}{1+\mu^2 B^2} \tag{5.4}$$

As the other contributions are not magnetic field dependent, we can just subtract a constant term in order to have $\Delta\sigma_{WAL}(B=0) = 0$. The different traces of $\Delta\sigma_{WAL}$ for different sample carrier densities $n_{hole}$ are displayed in fig. 5.6. It is to be noted that the size of the WAL peak is highly influenced by the carrier density.

The dependance on magnetic field of these WAL corrections to conductivity can be fitted with the following formula [5]:

$$\begin{aligned}\Delta\sigma_{WAL}(B_\perp) = &\frac{e^2}{2\pi^2\hbar}\left\{\Psi\left(\frac{1}{2}+\frac{B_\varphi}{B_\perp}+\frac{B_{SO3}}{B_\perp}\right)+\frac{1}{2}\Psi\left(\frac{1}{2}+\frac{B_\varphi}{B_\perp}+2\frac{B_{SO3}}{B_\perp}\right)-\frac{1}{2}\Psi\left(\frac{1}{2}+\frac{B_\varphi}{B_\perp}\right)\right.\\ &\left.-\ln\left(\frac{B_\varphi}{B_\perp}+\frac{B_{SO3}}{B_\perp}\right)-\frac{1}{2}\ln\left(\frac{B_\varphi}{B_\perp}+\frac{2B_{SO3}}{B_\perp}\right)+\frac{1}{2}\ln\left(\frac{B_\varphi}{B_\perp}\right)\right\}\end{aligned} \tag{5.5}$$

where $B_\perp$ is the out of plane magnetic field, $\Psi(X)$ is the digamma function, $B_\varphi$ is the phase coherence field and $B_{SO3}$ is a characteristic field of spin relaxation time due to cubic spin orbit interaction.

The first fitting parameter, $B_\varphi$, can be associated to a time, the phase coherence time $\tau_\varphi$ through the formula $\tau_\varphi = m^*/4\pi\hbar\mu n_{hole}B_\varphi$, $m^*$ being the heavy hole effective mass. The phase coherence time is the time the hole can travel through the lattice before loosing its coherence. It is of significant importance in weak antilocalization physic as any self

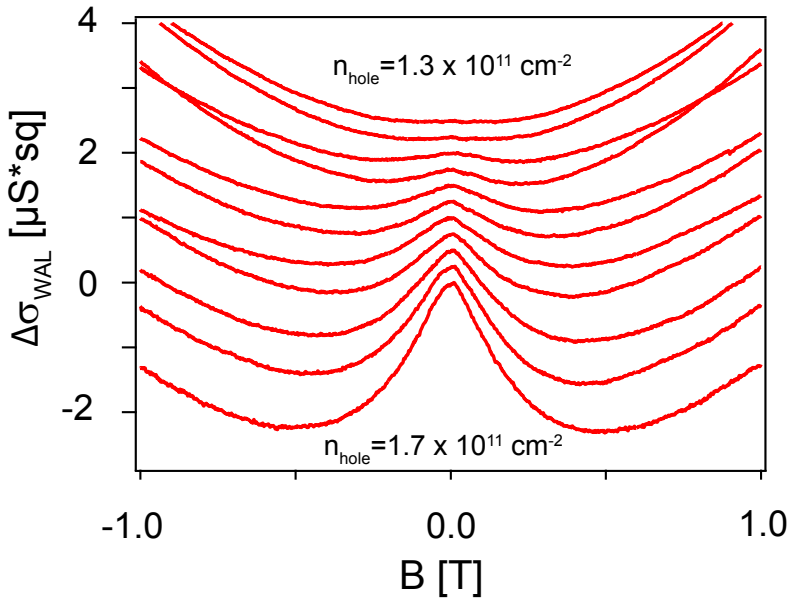


**Fig. 5.6:** Traces of the contribution of antilocalization on the channel conductivity $\Delta\sigma_{WAL}$ as a function of perpendicular magnetic field for different accumulation gate voltages ranging from $1.3 \times 10^{11}\text{cm}^{-2}$ (top trace) to $1.7 \times 10^{11}\text{cm}^{-2}$ (bottom trace). The antilocalization peaks disappears as carrier density is reduced (traces are offset for better visibility).

intersecting path for which the hole has to travel longer than $\tau_\varphi$ cannot contribute to WAL, given no interference will be possible at the end of the loop.

Similarly, the spin relaxation field can be associated to the spin relaxation time $\tau_{SO} = m^*/4\pi\hbar\mu n_{hole} B_{SO3}$, corresponding to a characteristic time of spin flipping mechanisms due to spin orbit interaction. The high spin orbit interaction limit mentioned in section 3.5.2 correspond to a spin orbit time $\tau_{SO}$ much larger than the average time between scattering events such as the spin direction undergoes a high number of small angle shifts across the loop.

Both these times can be compared the scattering time, $\tau_{tr} = m^*\mu/e$. This time represents the average time between two scattering events. Both $\tau_\varphi$ and $\tau_{SO}$ require to be orders of magnitude larger than $\tau_{tr}$ as $\tau_{tr}$ is directly related to the time required to travel across one of the weak antilocalization-inducing loop.

The dependance of $\tau_{tr}$, $\tau_{\varphi}$ and $\tau_{SO}$ on carrier density is displayed in fig. 5.7. Due to the low mobility of our sample, Shubnikov-de Haas oscillations could not be observed and the heavy hole effective mass could not be extracted so we used $m^* = 0.1 m_0$ where $m_0$ is the electron mass, consistently with what was observed in similar heterostructures [6–9]

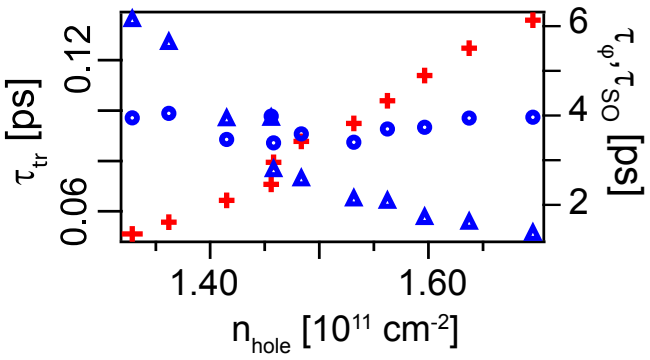


**Fig. 5.7:** Evolution of scattering time $\tau_{tr}$ (red crosses), phase relaxation time $\tau_{\varphi}$ (blue circles) and spin relaxation time $\tau_{SO}$ (blue triangles) as a function of carrier density

It is to be noted that the width of the weak antilocalization peaks measured is approximately two orders of magnitude larger than what is expected from similar heterostructure (see fig. 5.6) [10] and magneto-conductance experiments in general [11]. This can be explained by the low mobility of our device. The scattering time $\tau_{tr}$ measured being one order of magnitude smaller than in similar experiments, the weak antilocalization-inducing loops are expected to span an area two order of magnitude smaller. The magnetic field required to have a same amount of flux in these loops and break time reversal symmetry is then two order of magnitude larger.

The dependance of the characteristic times with respect to carrier density is indicative of the spin relaxation mechanism. In a sample with strong spin orbit interaction such as ours, D'Yakonov-Perel mechanism is expected. The spin orbit relaxation time $\tau_{SO}$ should then increase as the scattering time $\tau_{tr}$ and spin orbit splitting $\Delta_{SO}$ decreases ($\tau_{SO} \propto 1/(\tau_{tr} \times \Delta_{SO}^2)$ and $\Delta_{SO} = \alpha_3 E_z k_F^3$ where $\alpha_3$ is the cubic Rashba coupling, $E_z$ is the vertical electric field and $k_F$ is the Fermi wave number). The extracted values for the spin

orbit splitting energy is displayed in fig.5.8 and are consistent with values extracted in similar heterostructures [10, 7]

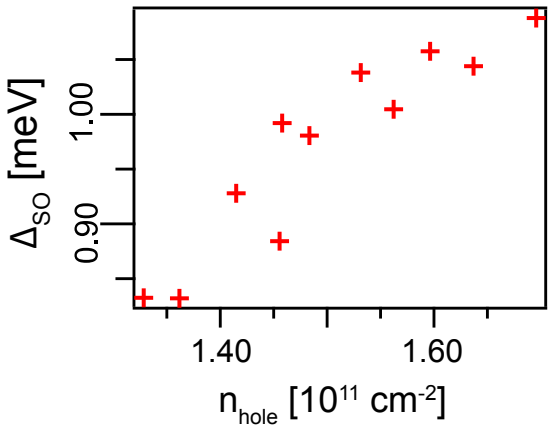


**Fig. 5.8:** Evolution of the spin splitting energy $\Delta_{SO}$ as a function of carrier density

### 5.2.3 Parallel magnetic field dependance

The sample was then rotated in the fridge in order to align the magnetic field in the plane of the 2DHG, perpendicular to the conduction channel (see fig.5.3). To the first order, breaking of the weak antilocalization in this configuration due to magnetic field is not expected as a parallel field induces no flux in the self intersecting paths, and thus should not break time reversal symmetry. Still, a peak in channel conductivity can be observed around 0 bias (see fig.5.9).

In order to make sure that this dependance is not induced by a misalignment of the sample in the magnetic field, it is possible to look at the Hall resistivity. The small magnetic field dependance of this resistivity (exclusively sensitive to out of plane magnetic field) allows us to extract a misalignment of only 2°(see fig.5.10). The small out of plane component of the magnetic field that this misalignment induces is not sufficient to explain the weak antilocalization breaking effect.

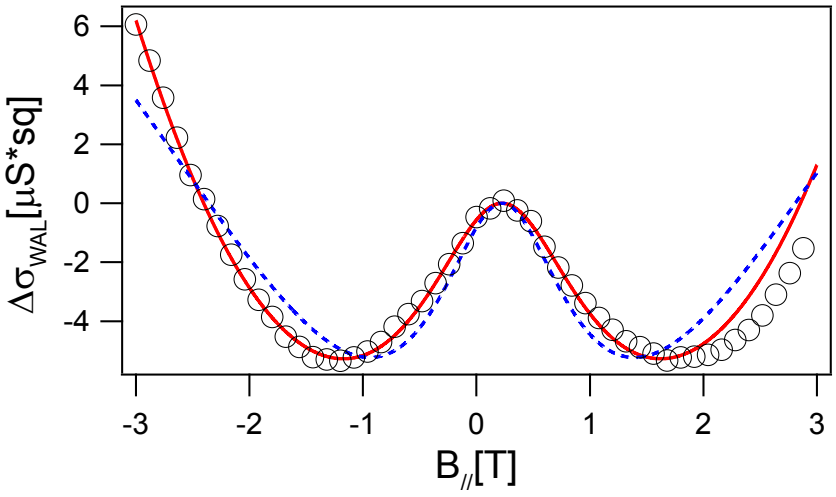


**Fig. 5.9:** Black circles: quantum correction to channel conductivity $\Delta\sigma_{WAL}$ as a function of in plane magnetic field. Fitting with the model from Minkov et al. [12] (blue dashed line) does not agree with our data without the addition of a $B_{//}^6$ (red line) term describing the virtual occupation of unoccupied subbands

A model had been developed by Minkov et al. [12] to explain this dependance of weak antilocalization on a parallel magnetic field. To do so, they took into account the effect of Zeeman splitting and surface roughness. We used the following formula to fit our data:

$$\Delta\sigma_{WAL}(B_{//}) = \frac{e^2}{4\pi^2\hbar}\left[2\ln\left(\frac{B_\varphi + B_{SO} + \Delta_r}{B_\varphi + B_{SO}}\right) + \ln\left(\frac{B_\varphi + 2B_{SO} + \Delta_r}{B_\varphi + 2B_{SO}}\right) - \ln\left(\frac{B_\varphi + \Delta_r + \Delta_s}{B_\varphi}\right) + S\left(\frac{B_\varphi + \Delta_r}{B_{SO}}\right) - S\left(\frac{B_\varphi}{B_{SO}}\right)\right] \tag{5.6}$$

with the $S(x)$ function being:

$$S(x) = \frac{8}{\sqrt{7+16x}}\left[\arctan\left(\frac{\sqrt{7+16x}}{1-2x}\right) - \pi\Theta(1-2x)\right] \tag{5.7}$$

and the $\Theta(y)$ function being the Heaviside step function. The effective fields $B_{SO}$ and $B_\varphi$ are the one extracted for this specific gate configuration at perpendicular field ($B_{SO}$ =

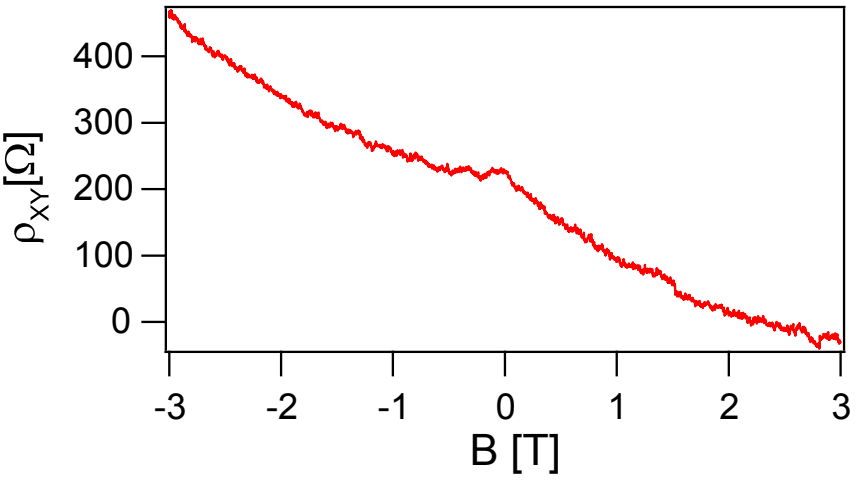


**Fig. 5.10:** Hall resistivity $\rho_{XY}$ as a function of in plane magnetic field. The small dependance on field indicates a tilt of the sample of only 2°.

170 mT, $B_\varphi$= 19 mT). The fitting parameters $\Delta_r$ and $\Delta_s$ are corrections made to $B_\varphi$ to take into account surface roughness and Zeeman splitting respectively, and are both expected to be proportional to $B_{//}^2$. The fitting was only done for the negative field half of the trace due to the asymmetry of the measurement, that can be explained by the Lorentz force applied on charge carriers[13, 14].

Still, as can be seen in fig.5.9 (blue dashed line), this formula does not fit our data correctly. For a better fit, we took into account the virtual occupation of higher subbands. While we consider that only one heavy hole subband is occupied in our system, virtual processes of occupation of higher subbands can break time reversal symmetry and induce weak antilocalization breaking[15]. These processes have to be taken into account as a supplementary term in $\Delta_r$ and have a $B_{//}^6$ dependance[11, 16], such as $\Delta_r = \Delta_{r1} + \Delta_{r2} = P \times B_{//}^2 + Q \times B_{//}^6$ where $P$ and $Q$ are fitting parameters.

This additional parameter allows for a much better fit of our data (see fig.5.9 red line). It also allows for 2DHG thickness extraction through the formula:

$$d \sim \left( \frac{Q \times \Phi_0^5}{\hbar^4 n_{hole}^2} \right)^{1/14} \tag{5.8}$$

where $d$ is the quantum well thickness, $Q$ the fitting parameter, $\Phi_0$ is the quantum of flux and $n_{hole}$ the carrier density. We then obtain a quantum well thickness of 8 nm, which is coherent with our epilayer thickness of 32 nm.

## 5.3 Conclusion

In this chapter, we presented magneto-transport measurements performed on a strained germanium quantum well confining a 2DHG at the $Ge/Al_2O_3$ interface. The 2DHG is induced by means of a negatively biased top gate. This measurements displayed signatures of weak antilocalization, with the magnetic field applied both perpendicular and parallel to the quantum well. We managed to extract characteristic parameters of the sample such as scattering time, phase coherence time, spin relaxation time or spin orbit splitting. Still, the sample was affected by a low mobility, that we explain by a high number of traps at the $Ge/Al_2O_3$ interface.

Our sample has the peculiar property of having the quantum well situated at the top interface, which is expected to allow for better spin control and easier fabrication process. On the contrary, this position of the quantum well requires more care during the fabrication process. The high number of traps is most likely due to the formation of a native germanium oxide on the top surface in between HF cleaning and ALD oxide deposition and germanium oxide is known to be a highly unstable oxide [17, 18].

For this reason, buried germanium heterostructures can provide a better option to achieve high mobility 2DHGs

# References


[1] Maksym Myronov, Andy Dobbie, Vishal A Shah, Xue-Chao Liu, Van H Nguyen, and David R Leadley. High quality strained ge epilayers on a si0. 2ge0. 8/ge/si (100) global strain-tuning platform. *Electrochemical and Solid-State Letters*, 13(11):H388–H390, 2010.

[2] J. P. Dismukes, L. Ekstrom, and R. J. Paff. Lattice parameter and density in germanium-silicon alloys1. *The Journal of Physical Chemistry*, 68(10):3021–3027, 1964.

[3] A. Dobbie, M. Myronov, R. J. H. Morris, A. H. A. Hassan, M. J. Prest, V. A. Shah, E. H. C. Parker, T. E. Whall, and D. R. Leadley. Ultra-high hole mobility exceeding one million in a strained germanium quantum well. *Applied Physics Letters*, 101(17):172108, 2012.

[4] Alessandro Crippa, Romain Maurand, Dharmraj Kotekar-Patil, Andrea Corna, Heorhii Bohuslavskyi, Alexei O. Orlov, Patrick Fay, Romain Laviéville, Sylvain Barraud, Maud Vinet, Marc Sanquer, Silvano De Franceschi, and Xavier Jehl. Level spectrum and charge relaxation in a silicon double quantum dot probed by dual-gate reflectometry. *Nano Letters*, 17(2):1001–1006, 2017. PMID: 28080065.

[5] SV Iordanskii, Yu B Lyanda-Geller, and GE Pikus. Weak localization in quantum wells with spin-orbit interaction. *ZhETF Pisma Redaktsiiu*, 60:199, 1994.

[6] C. Morrison, P. Wiśniewski, S. D. Rhead, J. Foronda, D. R. Leadley, and M. Myronov. Observation of rashba zero-field spin splitting in a strained germanium 2d hole gas. *Applied Physics Letters*, 105(18):182401, 2014.

[7] M. Failla, M. Myronov, C. Morrison, D. R. Leadley, and J. Lloyd-Hughes. Narrow heavy-hole cyclotron resonances split by the cubic rashba spin-orbit interaction in strained germanium quantum wells. *Phys. Rev. B*, 92:045303, Jul 2015.

[8] M. A. Zudov, O. A. Mironov, Q. A. Ebner, P. D. Martin, Q. Shi, and D. R. Leadley. Observation of microwave-induced resistance oscillations in a high-mobility two-dimensional hole gas in a strained ge/sige quantum well. *Phys. Rev. B*, 89:125401, Mar 2014.

[9] C. S. Wolfe, S. A. Manuilov, C. M. Purser, R. Teeling-Smith, C. Dubs, P. C. Hammel, and V. P. Bhallamudi. Spatially resolved detection of complex ferromagnetic dynamics using optically detected nitrogen-vacancy spins. *Applied Physics Letters*, 108(23):232409, 2016.

[10] Rai Moriya, Kentarou Sawano, Yusuke Hoshi, Satoru Masubuchi, Yasuhiro Shiraki, Andreas Wild, Christian Neumann, Gerhard Abstreiter, Dominique Bougeard, Takaaki Koga, and Tomoki Machida. Cubic rashba spin-orbit interaction of a two-dimensional hole gas in a strained-ge/sige quantum well. *Physical review letters*, 113(8):086601, 2014.

[11] D. M. Zumbühl, J. B. Miller, C. M. Marcus, K. Campman, and A. C. Gossard. Spin-orbit coupling, antilocalization, and parallel magnetic fields in quantum dots. *Phys. Rev. Lett.*, 89:276803, Dec 2002.

[12] G. M. Minkov, A. V. Germanenko, O. E. Rut, A. A. Sherstobitov, L. E. Golub, B. N. Zvonkov, and M. Willander. Weak antilocalization in quantum wells in tilted magnetic fields. *Phys. Rev. B*, 70:155323, Oct 2004.

[13] H. Sasaki, H. Ohno, S. Nishi, and J. Yoshino. Effect of tangential magnetic field on the two-dimensional electron transport in n-algaas/gaas superlattices and hetero-interfaces. *Physica B+C*, 117:703 – 705, 1983.

[14] A. A. Gorbatsevich, V. V. Kapaev, Yu. V. Kopaev, I. V. Kucherenko, O. E. Omel'yanovskii, and V. I. Tsebro. Magnetoresistance of an asymmetric quantum-size structure in

a parallel magnetic field: Field asymmetry independent of the current direction. *Journal of Experimental and Theoretical Physics*, 93(4):833–845, 2001.

[15] V I Fal'ko. Longitudinal magnetoresistance of ultrathin films and two-dimensional electron layers. *Journal of Physics: Condensed Matter*, 2(16):3797, 1990.

[16] Julia S. Meyer, Alexander Altland, and B. L. Altshuler. Quantum transport in parallel magnetic fields: A realization of the berry-robnik symmetry phenomenon. *Phys. Rev. Lett.*, 89:206601, Oct 2002.

[17] William L. Jolly and Wendell M. Latimer. The equilibrium ge(s) + geo2(s) = 2geo(g). the heat of formation of germanic oxide. *Journal of the American Chemical Society*, 74(22):5757–5758, 1952.

[18] Leo Brewer and Petros Zavitsanos. A study of the ge-geo2 system by an inductively heated dta apparatus. *Journal of Physics and Chemistry of Solids*, 2(4):284 – 285, 1957.

# Chapter 6

# Quantum point contacts in strained germanium heterostructure

The low-temperature electrical resistance resistivity of metals and semiconductors is usually determined by the scattering of carriers (electrons or holes) on scattering centers such as lattice defects or impurities. These scattering processes can be empirically incorporated in a Drüde model. For a given sample, it is then possible to define a characteristic length $l_{tr}$ called scattering length which is the mean distance a charge carrier will travel between two scattering events. But what about the case of a sample much smaller than this scattering length? The charge carriers would then travel through the sample without any scattering. This is called the ballistic regime.

A ballistic constriction connecting extended regions of a 2DHG is called a quantum point contacts (QPC). It consists of a number of one-dimensional channels whose contribution to the conductance is quantized. Upon modifying the confinement potential of a QPC, by the help of electrical gating for example, one could progressively open more and more of these one dimensional channels, thus leading to a staircase increase of the QPCs conductance. In the case of perfect transmission of the 1D modes, each conductance step should correspond to $2e^2/h$, i.e. twice the quantum of conductance $e^2/h = 38.8$ µS. The factor 2 accounts for spin degeneracy, which can be lifted by a sufficiently large Zeeman splitting at finite magnetic field.

The realization of such devices is a good indicator of the quality of a system, as a long enough $l_{tr}$ is a requirement for an experimental feasibility. It is also a useful tool to investigate physical properties of the system, as will now be explained.

## 6.1 Heterostructure and device fabrication

As it has been seen in chapter 5,having a 2DHG at the top surface of a heterostructure could present advantages in terms of spin manipulation and ease of fabrication process. However, the poor quality of the $Ge/Al_2O_3$ interface resulted in a rather low hole mobility.

Here we consider a new heterostructure in which the Ge quantum well is buried 70 nm below the surface. This heterostructure was also fabricated by the team of Maksym Myronov at Warwick University, with a similar recipe to the one described in chapter 5.1.1. The Ge layer is now 22 nm thick (as opposed to 32 nm) and it is capped by 70 nm of $Si_{0.2}Ge_{0.8}$, followed by 2 nm of silicon to prevent the oxidation of the $Si_{0.2}Ge_{0.8}$ (see Fig.6.1). In such a heterostructure, the 2DHG is once again situated in the germanium layer, which is now far enough from the top interface to limit the influence of imperfections and charged defects at the semiconductor-oxide interface. Additionally, the presence of the Si cap should prevent the formation of any germanium oxide in the device, thus improving even more the potential stability. Similar heterostructures have been shown to display exceptionally high mobilities, up to $10^6$ $cm^2/V.s$ [1–3].

The fabrication of the Hall bar sample measured in section 6.2 is in all point the same as the one described in section 5.1.2 except for one step. Due to the position of the 2DHG, buried under 70 nm of $Si_{0.2}Ge_{0.8}$, one etching step is added. During the ohmic contacts fabrication step, after optical lithography but before metallic evaporation, the sample is etched in a $Cl_2/N_2$ plasma for a depth of 75 nm. The design of the Hall bar is also slightly different, as shown in Fig.6.2.

On the other hand, fabrication of the QPC device measured in section 6.3 involves quite a few differences with the processes described earlier. Similarly to the fabrication of the Hall bars, the process starts with the deposition of alignment marks, made of 10/50

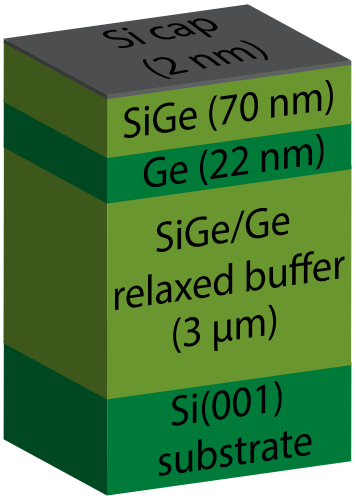


**Fig. 6.1:** Schematic of the heterostructure used in this chapter. On a silicon wafer is deposited a buffer layer of $Si_{0.2}Ge_{0.8}$. On top of this buffer layer, a 22 nm layer of Ge is deposited, then covered by 70 nm of $Si_{0.2}Ge_{0.8}$. Due to lattice mismatch the Ge layer is strained, thus inducing the formation of a 2DHG in it

nm of Ti/Au. We then proceed to mesa etching with the striking difference that in this device the mesa is much smaller, being made of two pads for the ohmic contacts linked by a 16 by 5 µm channel. This mesa is etched in a $Cl_2/N_2$ plasma for a depth of 100 nm. Then comes the fabrication of the ohmic contacts. Similarly to the fabrication process of the Hall bar made in the same heterostructure, after a step of optical lithography, the mesa is etched under the pads for a depth of 75 nm to attain the Ge layer. By metallic evaporation, 60 nm of platinum is then deposited to make the contacts. The sample is then cleaned in HF prior to deposition of 30 nm of $Al_2O_3$ by ALD.

Finally, the electrostatic gates are made in three lithography steps for better precision. First, the gate bonding pads are made by optical lithography as well as lines to get closer to the mesa, and 10/50 nm of Ti/Au is deposited (see Fig.6.3 left). Then, the fine gates are made by electron beam lithography (e-beam). They consist of one accumulation gate linking the two contacts that has a 300 nm wide constriction in the middle and of two side gates located 70 nm away from the constriction (see Fig.6.3 right). Here, 5/25 nm of Ti/Au are deposited. Finally, a link between the two aforementioned lithographies is

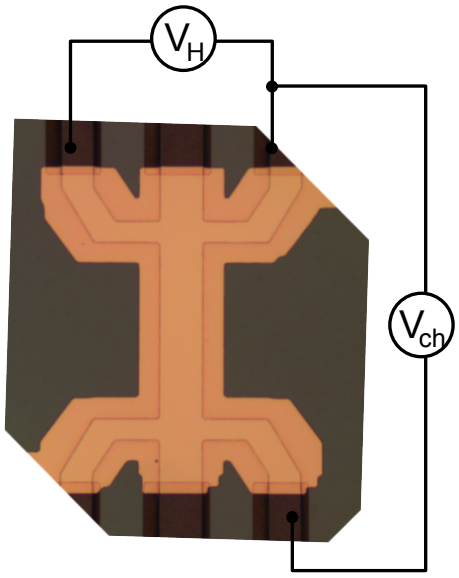


**Fig. 6.2:** Optical image of the Hall bar measured in this chapter. The points at which the channel bias $V_{ch}$ and the Hall bias $V_H$ are measured are also displayed

made by e-beam and 200 nm of Al. This metal has been chosen for its better conforming capacities to avoid breaking at the different physical steps at the fine gates, the mesa and the bonding pads.

## 6.2 Hall bar measurements

Prior to realizing QPCs, the transport characteristics of this heterostructure were investigated by magneto-transport measurements in a Hall bar device as described previously (see Fig.6.2). This also allowed us to validate the fabrication process. The measurement setup is the same as the one used in section 5.2.1, with no rotator.

The hole gas being frozen at low temperature, a negative voltage $V_{tg}$ is applied to the accumulation gate to study transport, the onset of conduction occurs near $V_{tg}$=-3.8 V. Due to risks of top gate leakage all the measurements have been performed on a top gate voltage range from -3.9 to -4 V.

Similarly to the experiment described in section 5.2.2, both the channel voltage $V_{ch}$ and the Hall voltage $V_H$ are measured as a function of magnetic field $B$ for different top gate

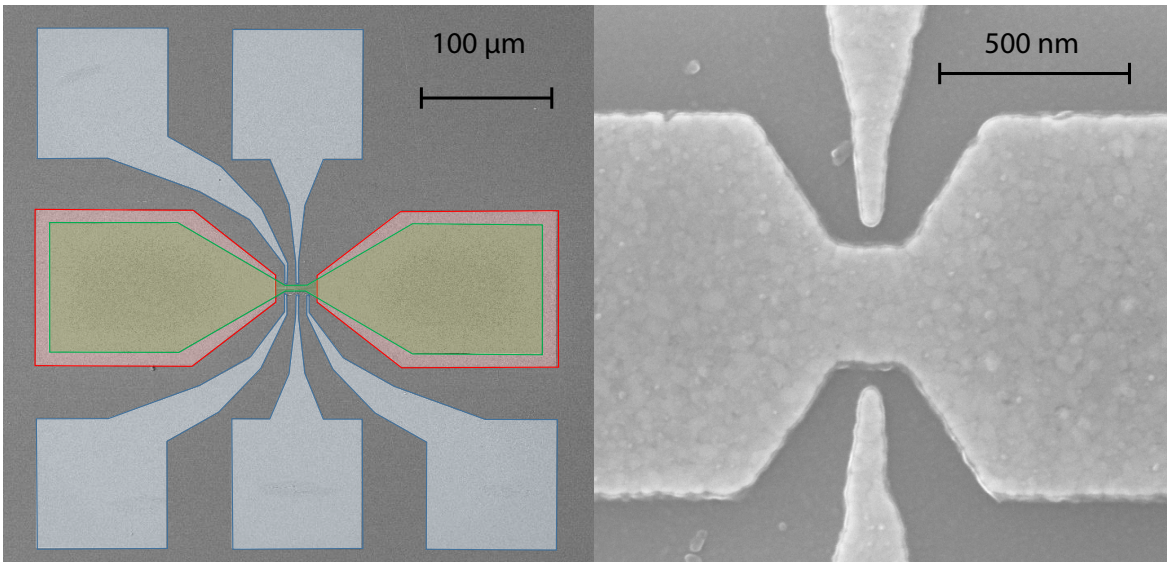


**Fig. 6.3: Left:** SEM image of the sample with added color showing the mesa (green), the ohmic contacts (red) and the bonding pads for the gates (blue, only three were connected to an actual gate) **Right:** Close SEM image showing the 300 nm wide constriction in the accumulation gate where the QPC is situated, as well as the two side gates situated at 70 nm of the constriction

voltages and the channel resistivity $\rho_{XX} = V_{ch}/(I_{ch}.N_{sq})$ and Hall resistivity $\rho_{XY} = V_H/I_{ch}$, where $I_{ch}$ is the current going through the channel and $N_{sq}$ represents the size of the channel in number of squares $N_{sq} = L/w$ where $L$ and $w$ are the channel length and width respectively. $N_{sq} = 4$ in this sample. Examples of the traces measured are displayed in fig.6.4. At high fields, traces of $\rho_{XX}$ show oscillations, corresponding to plateaus on the traces of $\rho_{XY}$. These oscillations are called Shubnikov-De Haas oscillations and are signatures of the quantum Hall effect [4]. From the linear dependence on $\rho_{XY}$ to magnetic field ( in low field region) we extract the carrier density $n_{hole}$ through the formula:

$$n_{hole} = \frac{B_\perp}{e \times \rho_{XY}(B_\perp)} \tag{6.1}$$

We can also estimate the carrier mobility $\mu$ from the channel resistivity at 0 field with the formula:

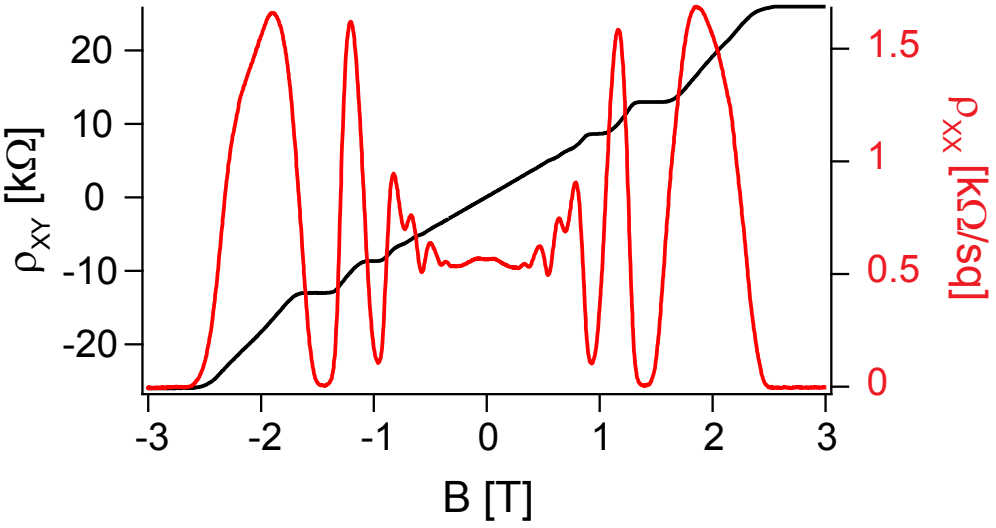


**Fig. 6.4:** Hall resistivity $\rho_{XY}$ (black) as well as channel resistivity $\rho_{XX}$ (red) as a function of magnetic field for $V_{tg}$= -3.9 V. The plateaus in $\rho_{XY}$ and the oscillations in $\rho_{XX}$ (Shubnikov-de Haas oscillations) are signatures of the quantum Hall effect. No weak antilocalization is observed

$$\mu = \frac{1}{e \times n_{hole} \times \rho_{XX}(B_{\perp} = 0)} \tag{6.2}$$

The values of $n_{hole}$ and $\mu$ obtained for different gate voltages are displayed in Fig.6.5. It is to be noted that while the carrier density obtained with this range of top gate voltage is slightly smaller than the ones obtained in section 5.2.2, the mobility measured is two orders of magnitude larger, reaching 170,000 $cm^2$/Vs and indicating a good interface quality. Further confirmation of this quality can be observed from the accumulation gate capacitance extracted from the carrier density dependence on $V_{tg}$ (53 nF/$cm^2$) being this time as much as half of the expected gate capacitance (109 nF/$cm^2$).

Looking at the traces of channel resistivity as a function of magnetic field, this time, no weak antilocalization is observed. This can be explained by the much higher mobility. Such an enhanced mobility implies a much longer scattering time while the spin relaxation time is in principles unchanged to first order. As a consequence, the requirement for weak antilocalization that the scattering time is much shorter than the spin orbit time may not be fulfilled anymore.

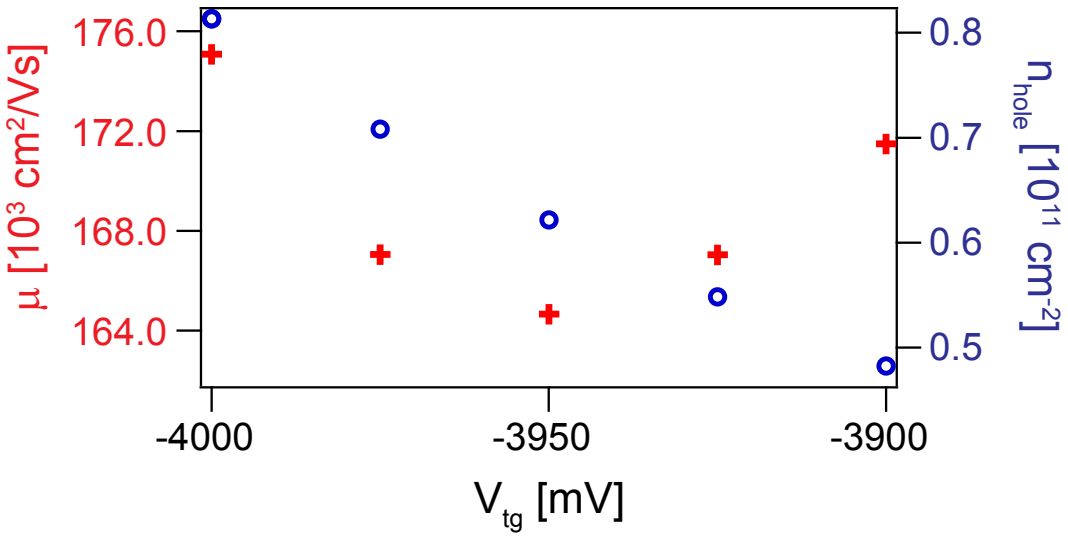


**Fig. 6.5:** Mobility $\mu$ (red crosses) as well as carrier density $n_{hole}$ (blue circles) as a function of accumulation gate $V_{tg}$

## 6.3 Quantum point contacts experiment

### 6.3.1 Quantization of conductance

The device studied here aims at showing the quantization of conductance in a germanium quantum well. This is done by creating a constriction in the 2DHG and varying its lateral size with the help of side electrostatic gates. Upon increasing the voltage on the side gates, the number of conducting one dimensional channels in the constriction decreases and the conductance of the system is expected to display a conductance step of $2e^2/h$ (at $B = 0$) each time a channel is pinched off.

Similarly to the experiments mentioned previously, the 2DHG is frozen at low temperature. A negative voltage is applied on the accumulation gate in order to induce the 2DHG and make the Ge quantum well conducting. A constriction is already created where the accumulation gate is narrower. A positive voltage $V_g$ is then applied on the side gates to deplete the 2DHG in the constriction (the two facing gates are always swept together). The conductance of the system is measured by using a lock-in with an AC excitation of 30 μV (well below the thermal broadening $E_{th}$ of the leads around the Fermi energy as

$E_{th} = 3.52 \times k_B T \approx 90$ μeV at 300 mK , with $k_B$ the Boltzmann constant and $T$ the electronic temperature [5]) and 0 DC bias between source and drain.

The conductance measured this way shows steps, but not of regular height. This is due to the presence of a series resistance, due to the RC filters present in the fridge (= 2.2 kΩ), the input resistance of the current amplifier (≈ 3 kΩ) and to the contact resistances in the device. If we consider an additional resistance $R_s$ in series of our QPC, the actual conductance of the QPC, $G$, can be obtained from measured conductance, $G_{meas}$:

$$G = \frac{1}{\frac{1}{G_{meas}} - R_s} \tag{6.3}$$

Correcting for a series resistance $R_s = 17$ kΩ and converting the conductance in units of $2e^2/h$ ($2e^2/h = 77$ μS), we recover regular steps of $2e^2/h$ as seen in Fig. 6.6.

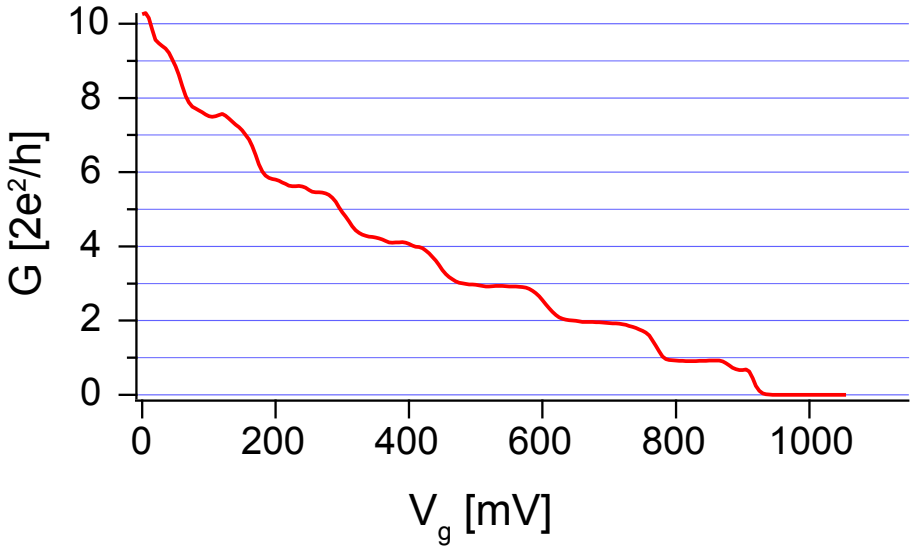


**Fig. 6.6:** Conductance $G$ in the QPC as a function of gates voltage $V_g$ showing conductance steps of $2e^2/h$. On the rightmost step, a kink can be observed, also known as the 0.7 anomaly

It is to be noted that the rightmost step possesses a kink at a value of conductance close to $0.7 \times 2e^2/h$. This feature, known as the 0.7 anomaly, has been the subject of extensive studies over the past years [6–8]. Still, there is no clear consensus about its origin, as many different explanations have been given (Kondo effect [9], inelastic scattering [10],

spontaneous spin polarization [11], etc...). Unfortunately, due to a small gate instability, this feature did not appear in all traces recorded, and its full characterization was not possible.

Another interesting characteristic of the trace displayed in Fig.6.6 is that only the first (rightmost) four steps are correctly aligned with integer multiples of $2e^2/h$. This implies that the series resistance is gate voltage dependent. This is coherent with the fact that a non negligible part of the series resistance is not due to the setup but comes from the sample (in this configuration, the setup should account for $5-6$ kΩ), on which the gates can have an influence.

### 6.3.2 Magnetic field dependence

We just saw how in a QPC, the conductance is quantized in steps of $2e^2/h$. This specific value is explained by the full transmission of a one dimensional mode ($e^2/h$) while the factor 2 is due to spin degeneracy. This means that applying a magnetic field should lift the degeneracy between the two spin degenerate levels and the $2e^2/h$ steps should become $e^2/h$ steps. This is indeed what is observed in Fig.6.7, showing conductance traces as a function of gate voltage $V_g$ for different magnetic fields applied perpendicular to the sample. The conductance as been corrected for series resistances of 17350, 21300, 20650, 20000, 19950 and 19600 Ω for magnetic fields of 0, 0.1, 0.2, 0.3, 0.4 and 0.5 T respectively. At 0.5 T, the $e^2/h$ steps are already clearly defined.

Since the splitting of the conductance steps with magnetic field is due to the Zeeman splitting of spin degenerate states, it is possible to extract the gyromagnetic ratio (or g-factor) of the hole spins. To do so, it is necessary to study the splitting of the steps with respect to magnetic field and to determine the lever-arm parameter relating the gate voltage to energy. In Fig.6.8, the transconductance $\partial G/\partial V_g$ of the device is displayed as a function of gate voltage $V_g$ (applied simultaneously on both gates) and magnetic field. No correction for the series resistance was made as it was not necessary in this case. The numerical derivative of the conductance with respect to gate voltage was done in order to turn step edges into peaks and more easily study their evolution. As we can see, each

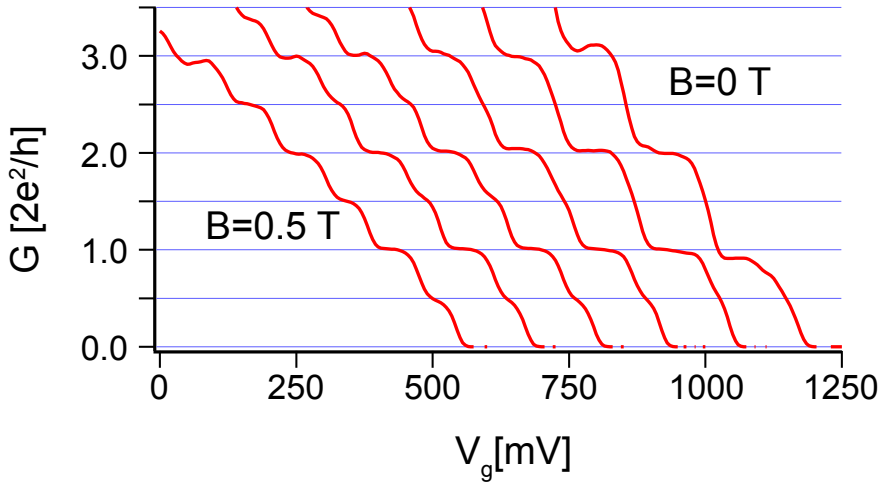


**Fig. 6.7:** Traces of device conductance $G$ as a function of gates voltage $V_g$ for different magnetic fields $B$ applied (traces are offset horizontally for better visibility), starting at 0T (rightmost trace) to 0.5 T (leftmost trace) in steps of 0.1 T. As the magnetic field is increased, the $2e^2/h$ steps split into $e^2/h$ steps due to Zeeman splitting of the subbands.

of the peaks at 0 field splits into two peaks of which the evolution is highlighted by blue dashed lines.

One noticeable feature in this map is the strong bending of the lines toward smaller gate voltages. This can be explained by an additional confinement induced by the perpendicular magnetic field. This confinement will turn the subbands into two dimensional Landau levels [12]. This bending makes it harder to extract the g-factor from high field data except from the splitting of the first conductance step.

There are different ways to extract the g-factor. One is to look at the bias dependence of the splitting of the step at a given magnetic field. Figure 6.9 shows such a dependence. This map has been obtained by measuring the device conductance as a function of both gate voltage $V_g$ and source drain bias $V_{sd}$ at a magnetic field of 0.5 T. Then the conductance has been renormalized by taking into account the serial resistance so that the trace at 0 bias shows steps of $e^2/h$ (at 0.5 T the splitting of the steps is well defined). The white number in Fig.6.9 indicates this conductance value in scale of $e^2/h$. Then the position of each data point on the bias axis has been modified to take into account this same series resistance. Indeed, due to series resistance, only a portion of the DC bias falls on the QPC.

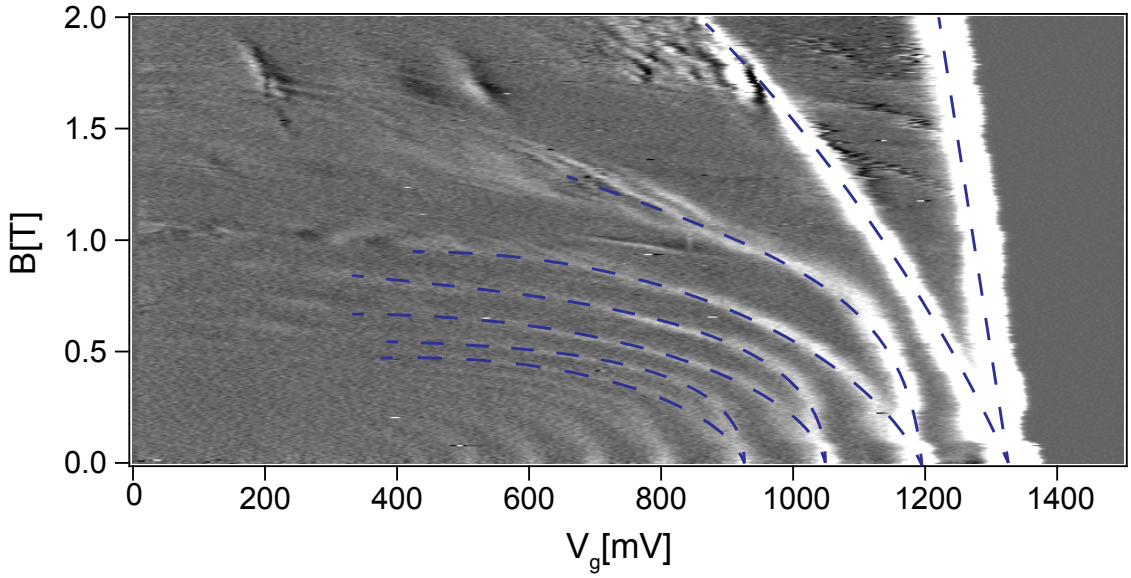


**Fig. 6.8:** Differential conductance $\partial G/\partial V_g$ as a function of gates voltage $V_g$ and magnetic field $B$. The blue dashed lines highlight the position of the peaks that are synonym of steps in the conductance $G$

The higher the conductance of the QPC and the larger the fraction of applied bias is falling on the series resistance. Each data point then has to be positioned on the graph for the actual value of bias accross the QPC. Finally, we take the derivative with respect to $V_g$ for a better visibility of each feature.

As shown in Fig.6.9, when increasing the bias, the conduction plateaus shorten, thus forming diamonds (highlighted by the yellow dashed lines). Similarly to the Coulomb diamonds described in section 2.1.4, we can extract a characteristic energy from the bias at which the diamond closes. In the case of the diamond for a plateau of an odd multiple of $e^2/h$, this energy corresponds to the Zeeman energy.

In our measurement, it is difficult to identify the exact position of the tip of the 1 $e^2/h$ plateau. The tip of the 3 $e^2/h$ plateau on the other hand (highlighted by the red dashed line) is more easily visible and its bias position doesn't seem so far off from the position of the tip of the 1 $e^2/h$ plateau. From there, we can then deduce a Zeeman energy of 0.54 meV. The g-factor $g$ can then be extracted from the formula:

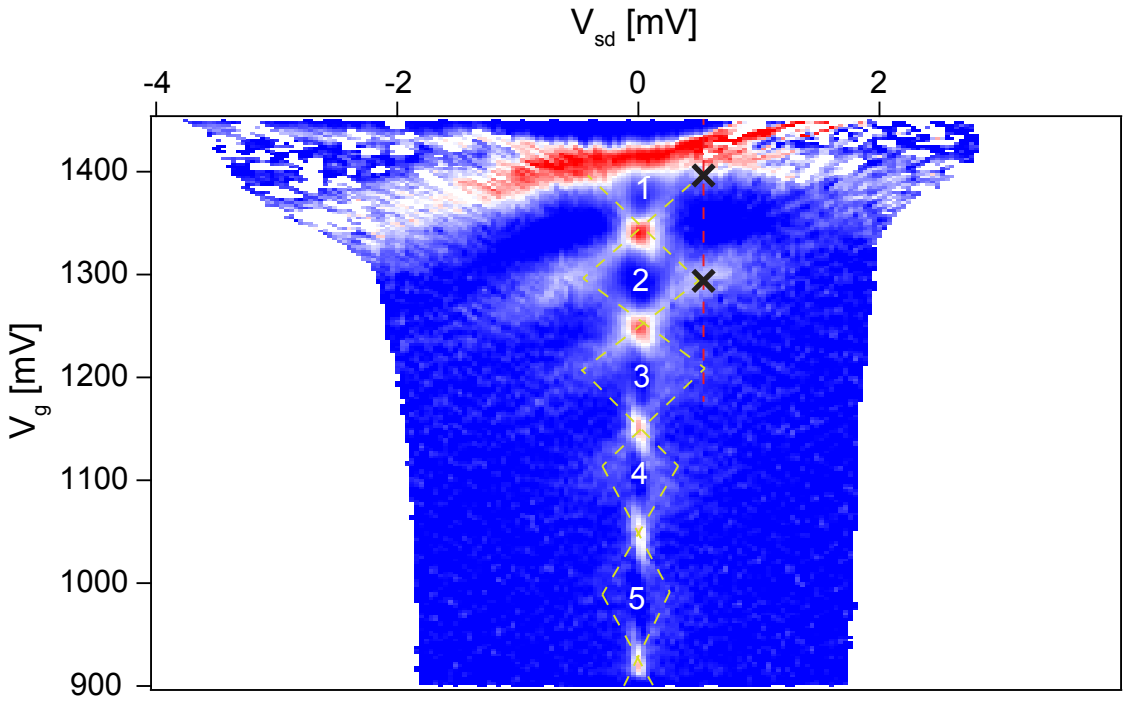


**Fig. 6.9:** Differential conductance $\partial G/\partial V_g$ a function of gates voltage $V_g$ and source drain bias $V_{sd}$ for an out of plane magnetic field B of 0.5 T. The yellow dashed lines highlight the position of peaks that are synonym of steps in the conductance G. These peaks form diamond shapes and the conductance is quantized inside them. The white numbers give the value of conductance in these plateaus in scale of $e^2/h$. The red dashed line highlight the bias position of the tip of the $3e^2/h$ diamond from which a g-factor of 19 is extracted. The black crosses highlight the gate splitting of the peak from which the gate lever arm is extracted.

$$g = \frac{E_z}{\mu_b B} \tag{6.4}$$

where $E_z$ is the Zeeman energy, $\mu_b$ the Bohr magneton and $B$ the magnetic field. We then obtain a g-factor for the splitting of the second $2e^2/h$ step $g = 19$.

A second way to obtain the g-factor is to study the field dependence of the gate splitting of the subbands, as seen in Fig.6.8. In this figure, we can see the linear dependence of the splitting with respect to magnetic field, giving a gate splitting value of $dV_g/dB = 172$ mV/T. This splitting then needs to be converted in energy. This requires the extraction of the gate lever arm. This can be done from the differential conductance map of Fig.6.9. As

mentioned earlier, each of the peaks situated at 0 bias (representing transitions from one plateau of conduction to the next) splits into two lines at non-zero bias. The dependence of this gate splitting with respect to bias is equal to the lever arm $\alpha$. For a given bias, such as the one previously mentioned of 0.54 mV for example, we measure a gate splitting of 102 mV (highlighted by the black crosses). This leads to a lever arm of $\alpha = 0.54/102 = 5.3\,10^{-3}$eV/V. We then obtain a g-factor of 15, using a new formula derivated from equation 6.4:

$$g = \frac{\alpha}{\mu_b}\frac{dV_g}{dB} \tag{6.5}$$

These two obtained values are consistent with each other, given the limited precision of the data extraction from the maps. They are also consistent with the theoretical value expected for g-factor of 21.4 for pure heavy holes in a germanium 2DHG [13]. In a QPC, the additional confinement is expected to reduce the g-factor which is consistent with our data [14].

## 6.4 Conclusion

In this chapter we started by characterizing a second germanium heterostructure. By the use of a Hall bar device, we measured the carrier density and mobility for different accumulation gate voltages, and obtained much higher mobility than for the previous heterostructure studied in chapter 5.

This high mobility allowed us to demonstrate quantization of conductance in a germanium QPC, which had never been reported before. From the splitting of the conductance steps with respect to magnetic field, we extracted two g-factor values of 19 and 15. The obtained g-factor values are close to the expected value for a pure heavy-hole subband in a Ge quantum well. Additionally, these values are quite high if compared to other two-dimensional structures based on other elements such as GaAs [15]. This large g-factor and high mobility can make germanium 2DHG an interesting platform for quantum spintronics and for Majorana fermions systems [16].

# References


[1] A. Dobbie, M. Myronov, R. J. H. Morris, A. H. A. Hassan, M. J. Prest, V. A. Shah, E. H. C. Parker, T. E. Whall, and D. R. Leadley. Ultra-high hole mobility exceeding one million in a strained germanium quantum well. *Applied Physics Letters*, 101(17):172108, 2012.

[2] Maksym Myronov, Christopher Morrison, John Halpin, Stephen Rhead, Catarina Casteleiro, Jamie Foronda, Vishal Ajit Shah, and David Leadley. An extremely high room temperature mobility of two-dimensional holes in a strained ge quantum well heterostructure grown by reduced pressure chemical vapor deposition. *Japanese Journal of Applied Physics*, 53(4S):04EH02, 2014.

[3] M. Myronov, C. Morrison, J. Halpin, S. Rhead, J. Foronda, and D. Leadley. Revealing the high room and low temperature mobilities of 2d holes in a strained ge quantum well heterostructures grown on a standard si(001) substrate. In *2014 7th International Silicon-Germanium Technology and Device Meeting (ISTDM)*, pages 11–12, June 2014.

[4] D. G. Seiler. *The Shubnikov-de Haas Effect: A Powerful Tool for Characterizing Semiconductors*, pages 578–587. Springer Berlin Heidelberg, Berlin, Heidelberg, 1989.

[5] P. Torresani, M. J. Martínez-Pérez, S. Gasparinetti, J. Renard, G. Biasiol, L. Sorba, F. Giazotto, and S. De Franceschi. Nongalvanic primary thermometry of a two-dimensional electron gas. *Phys. Rev. B*, 88:245304, 2013.

[6] S. M. Cronenwett, H. J. Lynch, D. Goldhaber-Gordon, L. P. Kouwenhoven, C. M. Marcus, K. Hirose, N. S. Wingreen, and V. Umansky. Low-temperature fate of the 0.7

structure in a point contact: A kondo-like correlated state in an open system. *Phys. Rev. Lett.*, 88:226805, May 2002.

[7] L. DiCarlo, Y. Zhang, D. T. McClure, D. J. Reilly, C. M. Marcus, L. N. Pfeiffer, and K. W. West. Shot-noise signatures of 0.7 structure and spin in a quantum point contact. *Phys. Rev. Lett.*, 97:036810, Jul 2006.

[8] S. Sarkozy, F. Sfigakis, K. Das Gupta, I. Farrer, D. A. Ritchie, G. A. C. Jones, and M. Pepper. Zero-bias anomaly in quantum wires. *Phys. Rev. B*, 79:161307, Apr 2009.

[9] Yigal Meir. The theory of the '0.7 anomaly' in quantum point contacts. *Journal of Physics: Condensed Matter*, 20(16):164208, 2008.

[10] A M Lunde, A De Martino, A Schulz, R Egger, and K Flensberg. Electron–electron interaction effects in quantum point contacts. *New Journal of Physics*, 11(2):023031, 2009.

[11] K. J. Thomas, J. T. Nicholls, M. Y. Simmons, M. Pepper, D. R. Mace, and D. A. Ritchie. Possible spin polarization in a one-dimensional electron gas. *Phys. Rev. Lett.*, 77:135–138, Jul 1996.

[12] K. F. Berggren, T. J. Thornton, D. J. Newson, and M. Pepper. Magnetic depopulation of 1d subbands in a narrow 2d electron gas in a gaas:algaas heterojunction. *Phys. Rev. Lett.*, 57:1769–1772, Oct 1986.

[13] Hannes Watzinger, Christoph Kloeffel, Lada Vukušić, Marta D. Rossell, Violetta Sessi, Josip Kukučka, Raimund Kirchschlager, Elisabeth Lausecker, Alisha Truhlar, Martin Glaser, Armando Rastelli, Andreas Fuhrer, Daniel Loss, and Georgios Katsaros. Heavy-hole states in germanium hut wires. *Nano Letters*, 16(11):6879–6885, 2016.

[14] M. Magdalena Gelabert and Lloren ç Serra. $g$-factor anisotropy of hole quantum wires induced by rashba interaction. *Phys. Rev. B*, 84:075343, Aug 2011.

[15] A. Srinivasan, L. A. Yeoh, O. Klochan, T. P. Martin, J. C. H. Chen, A. P. Micolich, A. R. Hamilton, D. Reuter, and A. D. Wieck. Using a tunable quantum wire to measure the

large out-of-plane spin splitting of quasi two-dimensional holes in a gaas nanostructure. *Nano Letters*, 13(1):148–152, 2013.

[16] Yuval Oreg, Gil Refael, and Felix von Oppen. Helical liquids and majorana bound states in quantum wires. *Phys. Rev. Lett.*, 105:177002, Oct 2010.

# Conclusion

As was described in the first chapter of this thesis, germanium is predicted to be a promising host material for quantum spintronics due to several properties. First of all, the spin of charge carriers in a germanium based device are expected to display a low hyperfine interaction with the nuclei spins, due to the low natural abundance of the only non-zero nuclear spin germanium isotope. The use of holes as charge carriers in such devices should reduce the influence of hyperfine interaction even more. Second of all, the spin orbit interaction, linking the electron's spin to its orbital motion, is predicted to be strong in germanium. This should allow for a better control of a spin state in a germanium based device through the use of EDSR.

The initial goal of the work described in this thesis was the realization of a quantum bit or qubit in a core shell Ge/Si nanowire. As described in chapter four, this led to the fabrication of double dot devices, confined by electrostatic gating. One of these devices allowed for the measurement of a double dot stability diagram, and of of the conductance resonances of this diagram showed signs of Pauli spin blockade, a requirement for the realization of spin qubits. Still, due to the extreme fragility and the lack of reproducibility of these devices, it was not possible to replicate these results. For this reason, it was then decided a change of host system, from Ge/Si core shell nanowires to germanium two dimensional heterostructures.

The heterostructure studied in chapter five has the peculiar property of having the hole quantum well situated at the top surface. This should allow for a more straightforward access to the two dimensional hole gas, both easing the fabrication process and permitting a easier use of superconducting contacts for induced superconductivity. Unfortunately,

the results displayed in chapter four also show that the formation of a native germanium oxide on the top interface will lead to the formation of numerous defects. These defects are the origin of the weak antilocalization signatures in the Hall bar devices studied in chapter five.

When trying to create nanoscale devices in these heterosctructures, the defects led to a great instability of the measurements. For this reason, chapter six describe experiments now performed on a heterostructure in which the germanium quantum well is buried under a SiGe layer. This allowed for the measurement of quantization of conductance in a germanium one dimensional channel, which had never been reported before. This is a very promising step toward the realization of qubits in germanium based devices.